



# Investigation on Fe-Co binary metal oxides supported on activated semi-coke for NO reduction by CO

Luyuan Wang <sup>a</sup>, Xingxing Cheng <sup>a,\*</sup>, Zhiqiang Wang <sup>a,\*</sup>, Chunyuan Ma <sup>a</sup>, Yukun Qin <sup>a,b</sup>

<sup>a</sup> National Engineering Lab for Coal-fired Pollutants Emission Reduction, Shandong Provincial Key Lab of Energy Carbon Reduction and Resource Utilization, Shandong University, Jinan, 250061, China

<sup>b</sup> School of Power Engineering, Harbin Institute of Technology, Harbin, 150001, China

## ARTICLE INFO

### Article history:

Received 30 April 2016

Received in revised form 7 August 2016

Accepted 9 August 2016

Available online 10 August 2016

### Keywords:

NO reduction

Carbon monoxide

Activated semi-coke

deNO<sub>x</sub> model reaction

*in situ* DRIFTS

## ABSTRACT

In this study, different amounts of Fe and Co species were loaded on activated semi-coke (ASC) using a hydrothermal method for the reduction of NO by CO. The series of prepared catalysts were characterized by SEM, N<sub>2</sub> physisorption, ICP, XRD, XPS, H<sub>2</sub>-TPR, and *in situ* DRIFTS, as well as ESR and Raman spectroscopy. In addition, the denitration (deNO<sub>x</sub>) performance and water/SO<sub>2</sub> resistance were investigated. The precursor solution with a molar ratio of 0.8:0.2 for Fe:Co (Fe<sub>0.8</sub>Co<sub>0.2</sub>/ASC) produced spherical clusters that were uniformly dispersed on the surface. Moreover, Fe<sub>0.8</sub>Co<sub>0.2</sub>/ASC exhibited the most effective deNO<sub>x</sub> activity. The highest deNO<sub>x</sub> activity for Fe<sub>0.8</sub>Co<sub>0.2</sub>/ASC (determined from the characterization) was attributed to the high fraction of Brønsted acid sites, high possibility for the formation of oxygen vacancies, and a strong redox performance. The DRIFTS results suggested a possible mechanism involving the adsorption of NO on the Fe<sub>0.8</sub>Co<sub>0.2</sub>/ASC surface, followed by its transformation to nitrates or nitrite/nitro species. At low temperatures (<200 °C), nitrates were predominantly adsorbed on the surface and could react with CO species, affording CO<sub>2</sub> and N<sub>2</sub>O. However, with increasing reaction temperatures (>200 °C), the coordinated nitrates and CO species on the surface reacted with the produced CO<sub>2</sub> and N<sub>2</sub>. The effects of water and SO<sub>2</sub> on the deNO<sub>x</sub> performance were examined. In the presence of only water, the deNO<sub>x</sub> performance decreased because of the competitive adsorption with NO, and in the presence of only SO<sub>2</sub>, reversible deactivation was observed; however, if both water and SO<sub>2</sub> were present, irreversible catalyst deactivation was observed.

© 2016 Published by Elsevier B.V.

## 1. Introduction

Nitrogen oxides (NO<sub>x</sub>) are primarily emitted from power plants, transportation, and other industrial sources. They considerably contribute to air pollution and are the cause of several environmental issues, such as acid rain, ozone depletion, greenhouse effects, and photochemical smog [1]. Because of the increasingly stringent emission regulations stipulated worldwide for NO<sub>x</sub>, the reduction of NO<sub>x</sub> emissions has gained extensive attention from both academia and industry. Moreover, selective catalytic reduction of NO<sub>x</sub> by NH<sub>3</sub> (NH<sub>3</sub>-SCR) has been demonstrated to be the most effective method for removing NO<sub>x</sub> from power plants [2]. However, this technology has several limitations, such as NH<sub>3</sub> leakage, catalyst poisoning, pipeline corrosion, and air preheater blockages; hence,

it is imperative to search for an alternative method to NH<sub>3</sub>-SCR [3,4].

In this regard, an alternative technology is the reduction of NO<sub>x</sub> by CO, which is developed from three-way catalyst (TWC) technology. Because CO is cost-effective, can be easily produced, and cannot generate solid carbon deposits in the CO + NO reaction, the application and investigation of the reduction of NO<sub>x</sub> by CO demonstrate significant potential for the substitution of NH<sub>3</sub>-SCR. However, there is an extremely low selectivity of interaction between CO and NO; thus, a significant amount of the gaseous reducing agent is oxidized by oxygen in the flue gas, which is not favorable for the deNO<sub>x</sub> process. To eliminate the negative impact of O<sub>2</sub>, some studies have proposed an integrated NO<sub>x</sub> adsorption-reduction process, which separates the interaction process into independent parts, *i.e.*, the interaction occurs in a special reactor where the adsorption of NO<sub>x</sub> is performed in the adsorption zone and adsorbed nitrogen oxides react with CO in reduction zones [3,5]. In addition, this process could promote the reduction of NO by CO applying in power plants. Furthermore, catalysts for this process

\* Corresponding authors.

E-mail addresses: [xcheng@sdu.edu.cn](mailto:xcheng@sdu.edu.cn) (X. Cheng), [jackywzq@sdu.edu.cn](mailto:jackywzq@sdu.edu.cn) (Z. Wang).

must exhibit a remarkable adsorption performance and excellent deNO<sub>x</sub> efficiency. Nevertheless, there are no suitable catalysts that exhibit these characteristics.

During the removal of NO<sub>x</sub> by CO, the key steps involve the adsorption of NO<sub>x</sub> and dissociation of NO [6]. The high efficiency of the removal process relies on the amount of surface oxygen vacancies, dispersion of metal oxides [7], and redox ability of catalysts [8] because an oxygen vacancy can activate the N–O bond to promote its dissociation. Additionally, a uniform dispersion and perfect redox ability can promote the adsorption of NO and oxidation of CO [9,10]. Noble metals (such as Pt, Pd, and Rh) supported on alumina or zeolite have long been considered as the most efficient catalysts for the NO + CO interaction; however, supported noble metal catalysts cannot be used in power plants for practical applications, which is attributed to their scarcity, high cost, low thermal stability, and non-renewable nature after inactivation [11]. Hence, significant efforts have been devoted to the search for cost-effective materials as alternatives to noble metals. Recently, a considerable number of studies have focused on the development of transition metal oxides assisted by rare earth oxides as transition metal oxides, especially copper, iron, cobalt and nickel oxides, exhibit excellent redox properties.

Iron-based catalysts [12,13] have been reported to exhibit a remarkable NO + CO interaction activity, and the catalytic activity of a metal oxide (10 wt%) supported on Al<sub>2</sub>O<sub>3</sub> and ZrO<sub>2</sub> for the NO + CO reactions decreases in the following order: Fe<sub>2</sub>O<sub>3</sub> > CuCr<sub>2</sub>O<sub>4</sub> > Cu<sub>2</sub>O > Cr<sub>2</sub>O<sub>3</sub> > NiO > Co<sub>3</sub>O<sub>4</sub> > MnO > V<sub>2</sub>O<sub>5</sub>; however, mono iron oxides are not efficient at low temperatures (<300 °C) [14]. Dong et al. [15] doped ceria into Fe/Ti<sub>0.5</sub>Sn<sub>0.5</sub>O<sub>2</sub>, which promoted the formation of polymeric Fe<sup>3+</sup> clusters (Fe<sup>3+</sup> clusters were more easily reduced to Fe<sup>2+</sup> under CO). The *in situ* diffuse reflectance infrared Fourier transform spectra (*in situ* DRIFTS) results indicated that Fe<sup>2+</sup> generated from the reduction of Fe<sup>3+</sup> was a primary active site for the NO + CO reaction. These results also suggested that the reaction occurred between adsorbed nitrates or coordinated nitrates and CO species. Cobalt can also exhibit an excellent performance for the removal of NO<sub>x</sub> by CO. According to previous studies, Co<sub>3</sub>O<sub>4</sub> [16], Co–CuO<sub>x</sub> [17], and Co-active carbon [18,19] exhibited an excellent deNO<sub>x</sub> efficiency, especially at low temperatures (<300 °C). Simonot et al. [16] reported that cobalt species could catalyze the cleavage of the N–O bond at low temperatures, which promoted the activity for the NO + CO reaction. However, most of the NO<sub>x</sub> decomposed to N<sub>2</sub>O by cobalt oxides. Liu et al. [17] investigated the synergistic effect in Cu–Co complex catalysts and demonstrated that the synergistic interaction between Co and Cu possibly played a significant role in the catalytic process. Moreover, Lv et al. [20] proposed that abundant surface synergistic oxygen vacancies (SSOVs) (Cu–□–Co) were present in binary metal catalysts, such as Cu–CoO<sub>x</sub>. The SSOVs were demonstrated to be the primary active components in the CO + NO reaction.

Nevertheless, for NO<sub>x</sub> adsorption, most catalysts in this process are zeolite-based which exhibit a low NO<sub>x</sub> adsorption capacity and a low catalytic activity at medium or low temperatures (<350 °C) [4]. Hence, the existing process cannot meet the requirements of power plants. Otherwise, low temperatures are beneficial for the adsorption of NO<sub>x</sub>; thus because of this characteristic, carbon-based catalysts are gaining attention. Carbon-based materials, such as commercial activated carbon, activated coke, and activated nanotubes, exhibit high surface areas, high pore volumes, and abundant active sites for the uniform dispersion of metal oxides, which assist catalysts, thereby rendering a comparatively high catalytic activity. These materials are also extremely stable at low temperature (<300 °C) [21,22]; hence, carbon-based materials are used as substrates in the majority of low-temperature deNO<sub>x</sub> catalysts. Semi-coke (SC), which is the byproduct obtained from the coking of lignite, has been used for the removal of SO<sub>x</sub>; it is a suitable

**Table 1**  
Elemental and proximate analysis results of SC.

Material	Elemental analysis (wt%)					Proximate analysis (wt%)			
	C	H	O	N	S	Moisture	Ash	Volatile	Fix carbon
SC	89.73	1.01	7.91	1.15	0.19	6.02	15.82	6.46	71.69

adsorbate and substrate for deNO<sub>x</sub> catalysis [23–25]. Noticeably, SC is cost-effective and exhibits high mechanical strength; in addition, its microstructure is developed. Hence, it exhibits a significant advantage over other carbonaceous candidates. SC activated by oxidizing acids (e.g., nitric acid) and loaded with transition metal oxides exhibits an extremely remarkable NO<sub>x</sub> adsorption capacity with an excellent NH<sub>3</sub>-SCR efficiency [26–29]. Moreover, carbon-based materials loaded with transition metals, such as Co [18,19], Cr [30,31], and Cu [32], also exhibit a high efficiency for the reduction of NO<sub>x</sub> by CO below 300 °C in the absence of O<sub>2</sub>.

Activated semi-coke (ASC) doped with metals exhibits a remarkable ability for the adsorption of nitrogen oxides [26,27], and if we optimize the surface metals on ASC, the catalysts can exhibit efficient deNO<sub>x</sub> performance at low temperatures. CO + NO catalysts were prepared using acid-activated SC as a supporting material, followed by the loading of two metals (Fe and Co) on SC. Considering that iron oxides are not efficient at low temperatures, and cobalt oxides exhibit high N<sub>2</sub>O selectivity, the CO + NO catalysts were hypothesized to exhibit an excellent deNO<sub>x</sub> performance (*i.e.* high NO conversion with low N<sub>2</sub>O selectivity) at low temperatures. For a better understanding of the interaction mechanism, the physicochemical properties of the catalysts were characterized by nitrogen physisorption, scanning electron microscopy (SEM), X-ray diffraction (XRD), X-ray photoelectron spectroscopy (XPS), temperature-programmed reduction of hydrogen (H<sub>2</sub>-TPR), and *in situ* diffuse reflectance infrared Fourier transform spectroscopy (DRIFTS). In addition, Raman spectroscopy and electron spin resonance (ESR) spectroscopy were used to explain the reaction path in the reduction zones.

## 2. Experimental methodology

### 2.1. Catalyst preparation

**Table 1** summarizes the properties of semi-coke (Shaanxi Shenmu Coal Mine Co., Ltd., China); it was first ground and sieved into granules with diameters of 1.02–1.27 mm (referred to as SC). Second, the SC particles were activated using nitric acid (30 wt%) at 80 °C for 2 h. After the particles were washed with deionized water, they were then dried at 120 °C for 6 h, followed by calcination in Ar at 700 °C for 4 h (referred to as ASC).

The metals were loaded onto ASC by the hydrothermal method. Ferric nitrate and cobalt nitrate (analytical-reagent grade, Sinopharm Chemical Reagent Co., Ltd) were dissolved in deionized water as the precursors. **Table 2** summarizes the loading amounts. Second, 5 g of ASC immersed in 30 mL of the precursor was transferred into a stainless steel autoclave. The autoclave was maintained at 160 °C for 24 h. Next, the activated coke particles were washed using deionized water and then dried at 120 °C for 6 h, followed by calcination in Ar at 700 °C for 4 h.

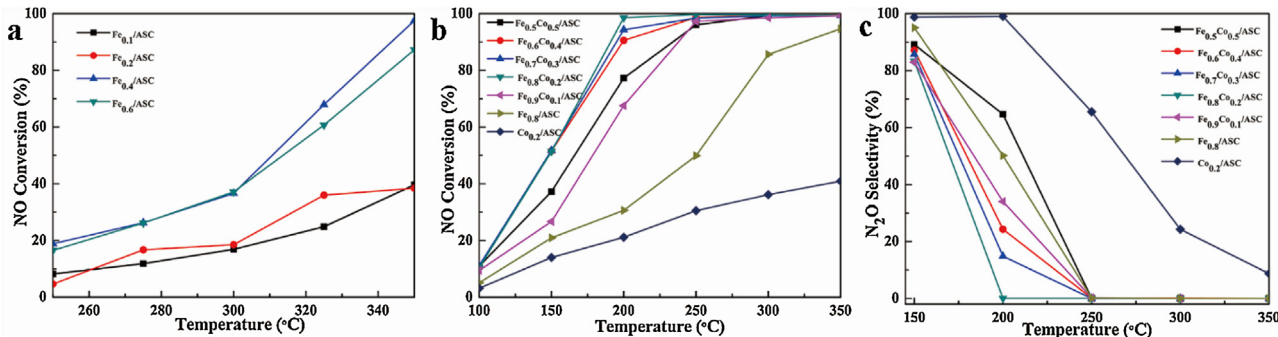
### 2.2. Catalytic activity

The activity of the prepared catalysts was investigated in a fixed-bed reactor system, which consisted of a stainless steel tubular reactor (i.d. of 12.7 mm), a gas supply and flow rate control unit (mass flow meter, Beijing Sevenstar Huachuang Electronics Co., Ltd.), a gas heating unit (furnace, Shandong Lulong furnace factory),

**Table 2**

Parameters and Textural properties of catalysts.

Catalysts	Concentration of precursor liquid (mol/L)	Fe loading wt.%	Co loading wt.%	Average pore width (nm)	Pore volume (cm <sup>3</sup> /g)	surface area (m <sup>2</sup> /g)
Fe <sub>0.8</sub> Co <sub>0.2</sub> /ASC	Fe(NO <sub>3</sub> ) <sub>3</sub> :1.653; Co(NO <sub>3</sub> ) <sub>3</sub> :0.413	5.58	1.49	2.14	0.590	272.096
Fe <sub>0.8</sub> /ASC	Fe(NO <sub>3</sub> ) <sub>3</sub> :1.653	2.04		1.76	0.590	333.021
Co <sub>0.2</sub> /ASC	Co(NO <sub>3</sub> ) <sub>3</sub> :0.413		0.39	1.74	0.590	359.996
ASC				1.83	0.567	463.986
Fe <sub>0.6</sub> /ASC	Fe(NO <sub>3</sub> ) <sub>3</sub> :1.240					
Fe <sub>0.4</sub> /ASC	Fe(NO <sub>3</sub> ) <sub>3</sub> :0.847					
Fe <sub>0.2</sub> /ASC	Fe(NO <sub>3</sub> ) <sub>3</sub> :0.423					
Fe <sub>0.1</sub> /ASC	Fe(NO <sub>3</sub> ) <sub>3</sub> :0.212					

**Fig. 1.** NO conversion (a, b) and N<sub>2</sub>O selectivity (c) of catalysts in the reduction of NO. Reaction conditions: 2000 ppm CO, 1000 ppm NO and balance by N<sub>2</sub>, GHSV = 6000 h<sup>-1</sup>.

a gas analysis unit (FTIR flue gas analyzer, Gasmet DX4000, Finland), and a data acquisition system. First, 2 g (approximately 5 cm<sup>3</sup>) of a sample was loaded in the reactor and pretreated by N<sub>2</sub> at 300 °C for 1 h, followed by cooling to room temperature. The total flow rate of the mixed gas was 500 mL/min (GHSV = 6000 h<sup>-1</sup>). The modeled flue gas was prepared from nitrogen, 1% NO balanced by N<sub>2</sub>, and 2% CO balanced by N<sub>2</sub> (Deyang Gas Ltd.). The test under each reaction condition was completed in greater than 1 h until to a steady state, and the data were collected after the outlet concentration reached a steady state. The NO conversion and N<sub>2</sub>O selectivity were calculated from concentrations of the inlet and outlet flue gases using Eqs. (1) and (2), respectively.

$$NO_{conversion} = \frac{[NO]_{in} - [NO]_{out}}{[NO]_{in}} \times 100\% \quad (1)$$

$$N_2O_{selectivity} = \frac{2 * [N_2O]_{out}}{[NO]_{in} - [NO]_{out}} \times 100\% \quad (2)$$

### 2.3. Catalyst characterization

The textural properties were evaluated by the physical adsorption of N<sub>2</sub> at 77 K using an automatic surface analyzer (Quantachrome Autosorb 1C), and the specific surface areas and pore volumes were calculated using density functional theory (DFT) from the N<sub>2</sub> adsorption/desorption isotherm. XRD patterns were recorded on a Rigaku D/max 2400 diffractometer using Cu-K $\alpha$  radiation ( $\lambda = 1.5056 \text{ \AA}$ ) at a scanning rate of 8°/min with a step size of 0.02° over the 2 $\theta$  range of 10–80°. The surface atomic states of the catalysts were analyzed by XPS (Axis Ultra<sup>DLD</sup>) with Al-K $\alpha$  radiation ( $h\nu = 1486.7 \text{ eV}$ , 225 W, 15 mA, 15 kV). The binding energies were calibrated using the C1 s peak at 284.5 eV as a reference, and experimental data were fitted with the Gaussian–Lorentzian mixed function as implemented in the Casa XPS software. The surface morphologies of the samples were observed by field-emission scanning electron microscopy (SEM, Hitachi S-4800). Raman scattering

measurements were conducted using a multichannel modular triple Raman system (JY-HR800, 532 nm, 0.3 mW) with confocal microscopy from 100 cm<sup>-1</sup> to 1000 cm<sup>-1</sup>. The concentrations of the loaded metals were measured by ICP-AES (OPTIMA 7000DV, Perkin Elmer). Before testing, all samples were ground into fine powder and dissolved using aqua regia. The surface oxides tests were performed on a X-ray fluorescence instrument (Thermo Scientific™ ARL QUANTX EDXRF). The temperature-programmed reduction of hydrogen (H<sub>2</sub>-TPR) was performed using a Chemisorb instrument (Chembet Pulsar TPR/TPD 2139). These tests were conducted using a quartz U-type reactor, which was connected to a thermal conductivity detector. The module reductant gas was composed of 10 vol% H<sub>2</sub> balanced by Ar at a flow rate of 40 mL/min. Before reduction, the sample (100 mg) was pretreated in a N<sub>2</sub> stream at 300 °C for 1 h, and then the TPR began from room temperature to 900 °C at a rate of 10 °C/min. Electron spin resonance (ESR) spectra were recorded on an ESR spectrometer (JEOL JES-FA 200) at a scan range of 0–1000 mT and a microwave frequency ranging from 9100 to 9300 MHz. The spectra were recorded at –100 °C, and the electron spin factor 'g' was calculated using Eq. (3).

$$g = 0.07148 \times \frac{F(\text{MHz})}{H(\text{mT})} \quad (3)$$

In Eq. (3), F represents the microwave frequency (in MHz) and H represents the magnetic field intensity (in mT).

Moreover, *in situ* DRIFTS spectra were recorded from 650 cm<sup>-1</sup> to 4000 cm<sup>-1</sup> at a spectral resolution of 4 cm<sup>-1</sup> (number of scans = 100) on a Nicolet 6700 FTIR spectrophotometer equipped with a high-sensitivity MCT detector cooled by liquid N<sub>2</sub>. The DRIFTS cell (Pike) was fitted with a ZnSe window and heating cartridge, which permits heating the sample to 500 °C. The catalysts (approximately 25 mg) were ground into a fine powder (<2  $\mu$ m) and placed on a sample holder; they were carefully flattened for IR reflection. The sample was pretreated with a high-purity Ar stream at 400 °C for 1 h to eliminate the physically absorbed water and

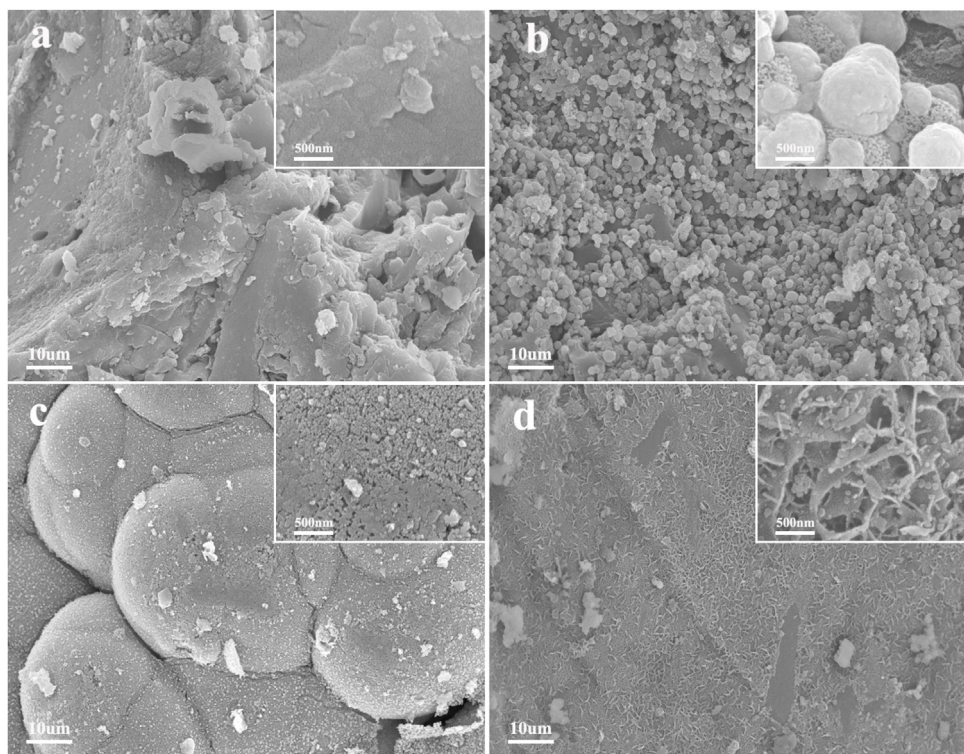


Fig. 2. SEM images of catalysts (a) ASC, (b) Fe<sub>0.8</sub>Co<sub>0.2</sub>/ASC, (c) Fe<sub>0.8</sub>/ASC and (d) Co<sub>0.2</sub>/ASC.

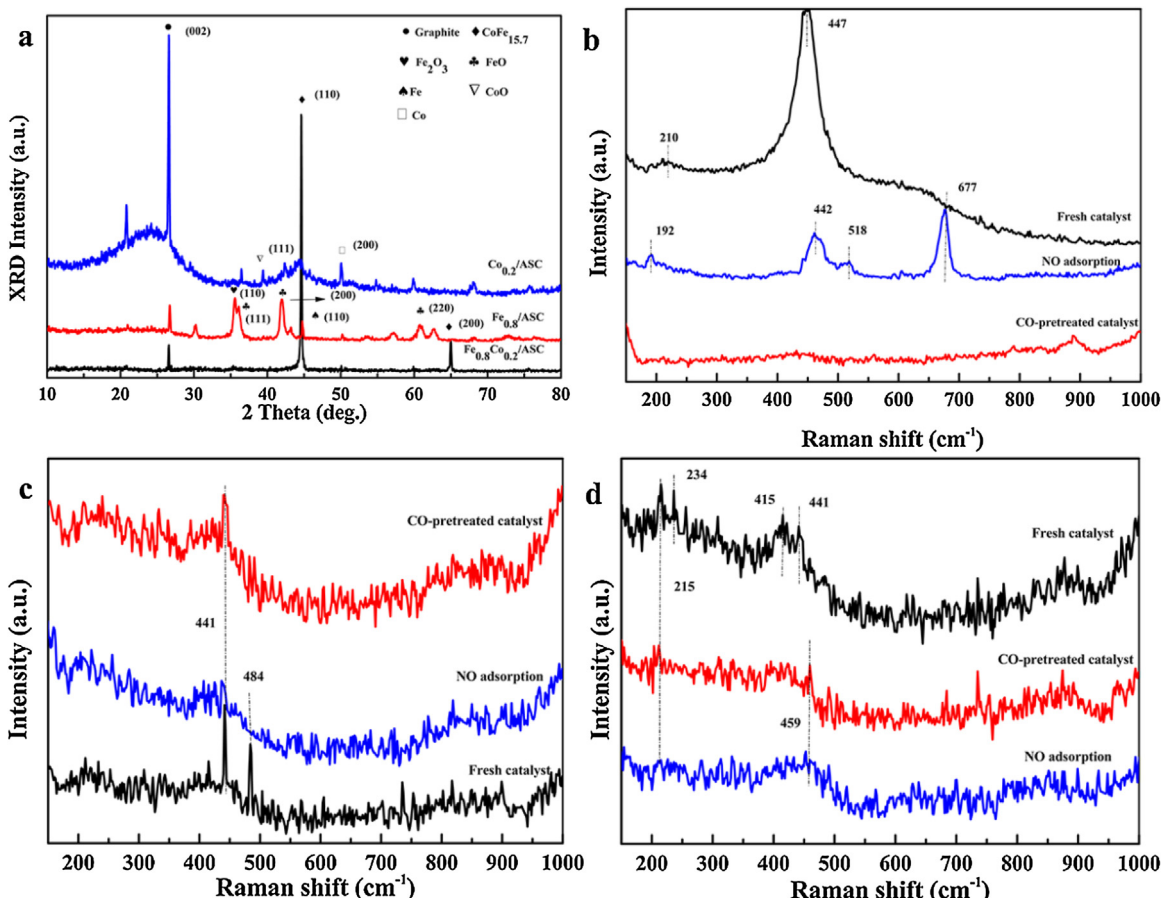
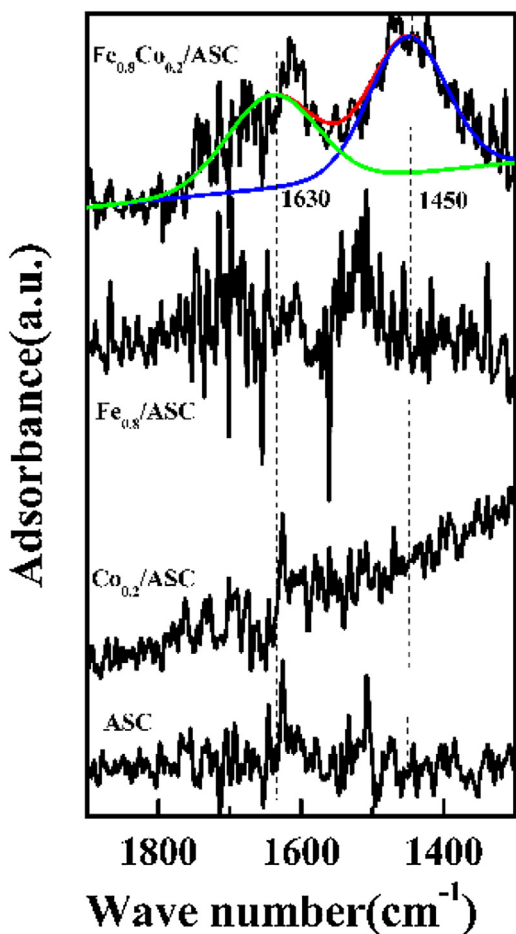


Fig. 3. XRD patterns of catalysts (a) and Raman spectra of catalysts (b)Fe<sub>0.8</sub>Co<sub>0.2</sub>/ASC, (c) Fe<sub>0.8</sub>/ASC and (d) Co<sub>0.2</sub>/ASC.



**Fig. 4.** DRIFTS spectra of catalysts exposed to 1000 ppmNH<sub>3</sub>/Ar at 100 °C for 30 min.

other impurities. At each target temperature, the sample background was collected during cooling. At each desired temperature, the sample was exposed to a controlled stream of 2000 ppm CO and/or 1000 ppm NO balanced by Ar at a flow rate of 100 mL/min for 0.5 h for saturation. The spectra were recorded at various target temperatures by subtracting the corresponding background reference.

### 3. Results and discussion

#### 3.1. Catalytic performance

Catalysts with different metal loadings were prepared, and Fig. 1 shows their catalytic activities for the reduction of NO by CO. For all the prepared catalysts, the NO reduction efficiency increased with temperature. The NO conversion of the catalyst loaded with only Fe reached approximately 80% at a temperature above 300 °C (Fig. 1(a)). The catalytic activity increased when the concentration of the ferric nitrate precursor solution increased from 0 to 1.033 mol/L; when the concentration surpassed 1.033 mol/L, no enhancement was observed for the NO conversion. From these results, the optimal concentration was concluded to be ~1.033 mol/L for ASC loaded only with Fe. In Fig. 1(b), the Co loading caused a significant improvement of the catalytic activity at low temperatures and when equimolar amounts of Fe and Co were co-loaded onto ASC; the denitration efficiency attained ~80% at only 200 °C. Thus, the total metal ion molar concentration for the precursor solution was selected as 2.066 mol/L. Catalysts loaded with only a single metal, either Fe or Co, exhibited very low cat-

alytic activities for the reduction of NO by CO. For both catalysts, the NO conversion was less than 50% at temperatures up to 250 °C. Next, Fe and Co were then co-impregnated on the catalysts with Fe:Co ratios ranging from 0.6:0.4 to 0.9:0.1; this loading range of Co and Fe resulted in the dramatic enhancement of the NO reduction activity, especially at low temperatures. For these bi-metal catalysts, a NO conversion above 95% was observed at 250 °C. Among all of the prepared catalysts, the Fe<sub>0.8</sub>Co<sub>0.2</sub>/ASC catalyst exhibited the best deNO<sub>x</sub> activity; thus, it was selected for further discussion of the reaction mechanisms. Notably, a NO conversion of approximately 100% was obtained over the selected Fe<sub>0.8</sub>Co<sub>0.2</sub>/ASC catalyst at temperatures as low as 200 °C.

For NO reduction, NO is reduced to either N<sub>2</sub>O or N<sub>2</sub> [16]. Fig. 1(c) shows the N<sub>2</sub>O selectivity for different catalysts at different temperatures. The decreased N<sub>2</sub>O selectivity demonstrates the increment of the N<sub>2</sub> yield, which in turn indicates good deNO<sub>x</sub> performance. At temperatures below or equal to 150 °C, the N<sub>2</sub>O selectivities were greater than 80% for all the prepared catalysts. Most of the converted NO was reduced to N<sub>2</sub>O, instead of the harmless N<sub>2</sub>. Thus, the prepared ASC catalysts should be used above 200 °C. For most catalysts, the N<sub>2</sub>O selectivity exhibited a trend opposite to that exhibited by the NO conversion. The higher the NO conversion, the lower the N<sub>2</sub>O selectivity. Zero N<sub>2</sub>O selectivity (implying 100% reduction to N<sub>2</sub>) was achieved by the Fe<sub>0.8</sub>Co<sub>0.2</sub>/ASC catalyst at 200 °C. The catalysts with good catalytic activities for the NO + CO reaction tended to exhibit good capabilities for reducing NO further to N<sub>2</sub>. N<sub>2</sub>O was speculated to be an intermediate in the NO + CO reaction [12,13]. The detailed reaction mechanism would be further analyzed by *in situ* DRIFTS.

#### 3.2. Surface morphology of the prepared catalysts

Fig. 2 shows the surface morphologies of some representative catalysts, viz., catalyst support, catalysts loaded with Fe, catalysts loaded with Co, and catalysts co-impregnated with both Fe and Co. The surface of the ASC support exhibited a carbon foliated structure. When Fe was loaded onto the ASC support, the Fe<sub>0.8</sub>/ASC catalyst exhibited a block-like structure with aggregates of metal oxide clusters on the surface [15]. The morphology of Co<sub>0.2</sub>/ASC was quite different, exhibiting a dispersed leaf-like structure; an analogous morphology was previously proposed [33,34]. When both Fe and Co were impregnated, large spherical clusters were observed on the surface. The surface morphology significantly changed by the co-impregnation of Co and Fe. This special spherical structure could be attributed to the mixed crystal effect [35]. Fe(OH)<sub>3</sub> and Co(OH)<sub>3</sub>, hydrolyzed from nitrate by hydrothermal treatment, exhibited similar lattice structures [36,37]. Thus, when Fe and Co were co-impregnated, one of the metals was possibly incorporated into the lattice of the other. This synergistic effect can also cause incremental metal doping.

#### 3.3. Metal loading content and textural characteristics

Table 2 summarizes the results obtained from ICP and the textural parameters of the representative catalysts. By comparing the ICP results, a significant difference was observed between the binary metal catalysts and the mono-metal catalysts, i.e., the Fe and Co content of Fe<sub>0.8</sub>Co<sub>0.2</sub>/ASC was greater than that of Fe<sub>0.8</sub>/ASC and Co<sub>0.2</sub>/ASC, respectively. This observation was confirmed by the analysis described in Section 3.2: the synergistic effect of Fe and Co possibly caused the increased metal loading.

For textural data, the increment of metal oxides resulted in a clear decrease of the average specific surface area. The surface area of ASC was as high as 463.9 m<sup>2</sup>/g. Nevertheless, Fe<sub>0.8</sub>Co<sub>0.2</sub>/ASC exhibited a specific surface area of only 272.0 m<sup>2</sup>/g, while those of Fe<sub>0.8</sub>/ASC and Co<sub>0.2</sub>/ASC were in between. Notably, the average pore

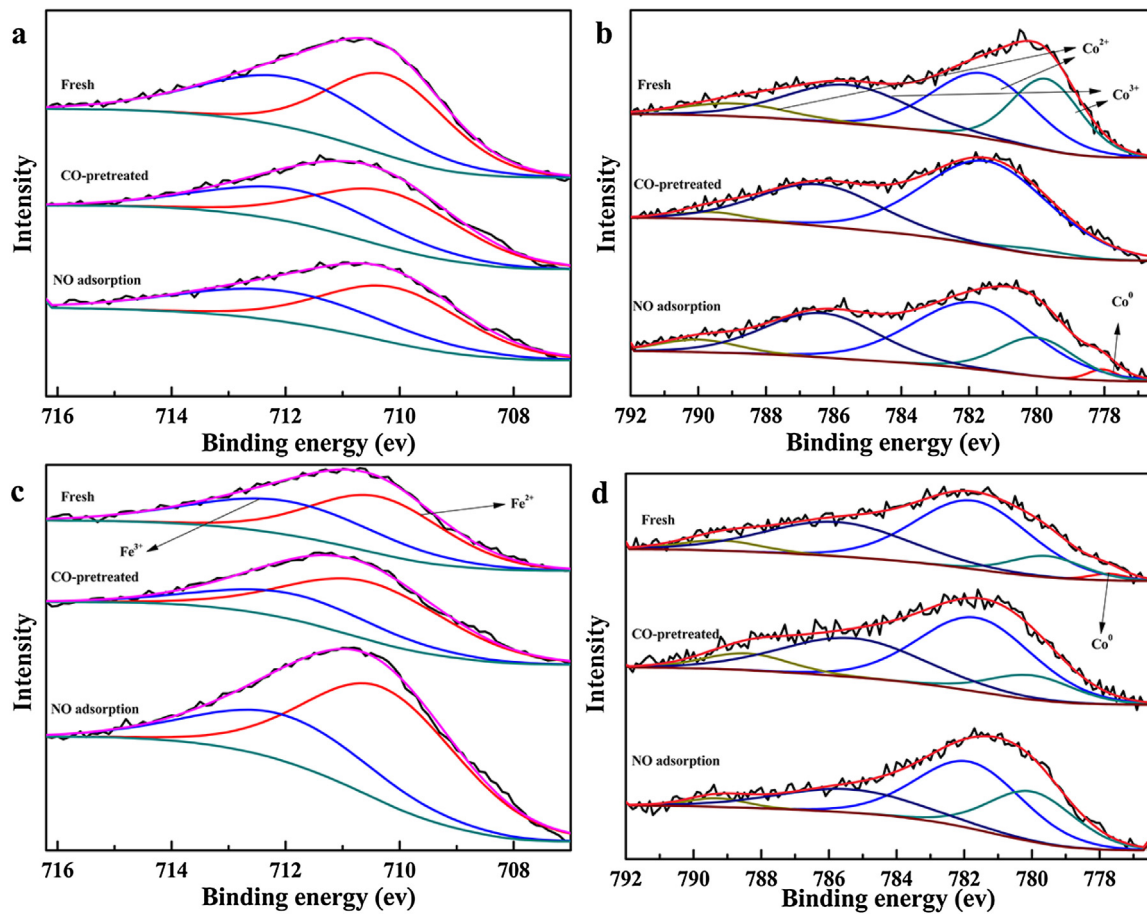


Fig. 5. Fe 2p<sub>3/2</sub> and Co 2p<sub>3/2</sub> from XPS spectra of catalysts (a, b) Fe<sub>0.8</sub>Co<sub>0.2</sub>/ASC, (c) Fe<sub>0.8</sub>/ASC, (d) Co<sub>0.2</sub>/ASC with different treatment.

width of Fe<sub>0.8</sub>Co<sub>0.2</sub>/ASC was 2.14 nm, which was greater than the pore width of the ASC support (1.83 nm). The spherical clusters on the Fe<sub>0.8</sub>Co<sub>0.2</sub>/ASC catalyst possibly generated several new types of pore structures. Nevertheless, the total pore volume of all the investigated catalysts was similar. To further understand the cause of this phenomenon, the N<sub>2</sub> adsorption–desorption isotherms and pore size distribution curves of the representative catalysts were investigated, and Fig. S1 and S2 show the respective results. According to the International Union of Pure and Applied Chemistry (IUPAC) classification, all ASC-supported catalysts exhibited a combination of type I and type IV isotherms (Fig. S1). At a relative pressure below 0.1, the isotherms exhibited a sharp increase, with specific type I isotherm characteristics. This period of the curve was associated with micropores [38]. In contrast, at intermediate and high relative pressures, the curves exhibited clear type IV isotherms with hysteresis loops of types A and B, indicating that a significant amount of mesopores were present in the ASC-supported catalysts [39,40]. Furthermore, the pore size distribution curves (Fig. S2) were analyzed; for all catalysts, a strong narrow peak was observed at pore widths ranging from 0.5 to 1.5 nm. The intensity of this peak continuously decreased with the increasing total loading of the metal oxides. In addition to this strong peak, a shoulder peak with a slightly larger pore width was observed for all catalysts, and the peak shifted to larger pore sizes with increased loading. It is hypothesized that the loaded metals would occupy some pore structure, resulting in a decrease of the number of micropores. However, for the four catalysts, the peak at approximately 5 nm exhibited almost no variation, indicating that pores of this size were not affected by the metal loading. Distinct from the other catalysts, Fe<sub>0.8</sub>Co<sub>0.2</sub>/ASC exhibited three weaker and wider peaks at pore widths ranging

from 10 to 20 nm. As speculated above, several new types of pore structures were produced on the Fe<sub>0.8</sub>Co<sub>0.2</sub>/ASC surface. Thus, the Fe<sub>0.8</sub>Co<sub>0.2</sub>/ASC catalyst exhibited less pores, albeit with a larger pore size. The large pore size and high loading of Fe<sub>0.8</sub>Co<sub>0.2</sub>/ASC were expected to improve deNO<sub>x</sub> efficiency.

#### 3.4. XRD and Raman analysis

Fig. 3(a) shows the XRD results of three representative catalysts (Fe<sub>0.8</sub>Co<sub>0.2</sub>/ASC, Fe<sub>0.8</sub>/ASC, and Co<sub>0.2</sub>/ASC). For all catalysts, a diffraction peak was observed at approximately 25–30°, which was a peak characteristic for the (002) crystal face of graphite (JCPDF=13-0148); this characteristic peak decreased with increased metal loading. Notably, characteristic peaks of iron oxides and cobalt oxides were not observed for Fe<sub>0.8</sub>Co<sub>0.2</sub>/ASC, but a clear peak was observed for CoFe<sub>15.7</sub> (JCPDF=65-7519). Thus, there was a mixed crystal effect in co-impregnation. In the XRD pattern of Fe<sub>0.8</sub>/ASC, some characteristic peaks for iron species were detected, such as Fe<sub>2</sub>O<sub>3</sub> (JCPDF=24-0072), FeO (JCPDF=03-0968), and Fe (JCPDF=01-1262). In contrast, characteristic peaks of CoO (JCPDF=48-1719) and zero-valent Co (JCPDF=15-0806) were observed for Co<sub>0.2</sub>/ASC. No other peaks for cobalt species were observed.

Raman spectroscopy is a potential method for detecting the arrangement of metal oxides for obtaining some additional structure information, which cannot be obtained by XRD. Figs. 3(b–d) show the Raman spectra of catalysts under different treatment conditions. CO-pretreated catalysts were purged with 2000 ppm CO (GHSV=6000 h<sup>-1</sup>) at 300 °C for 30 min, while NO-adsorbed catalysts were prepared by purging the catalysts with 2000 ppm CO

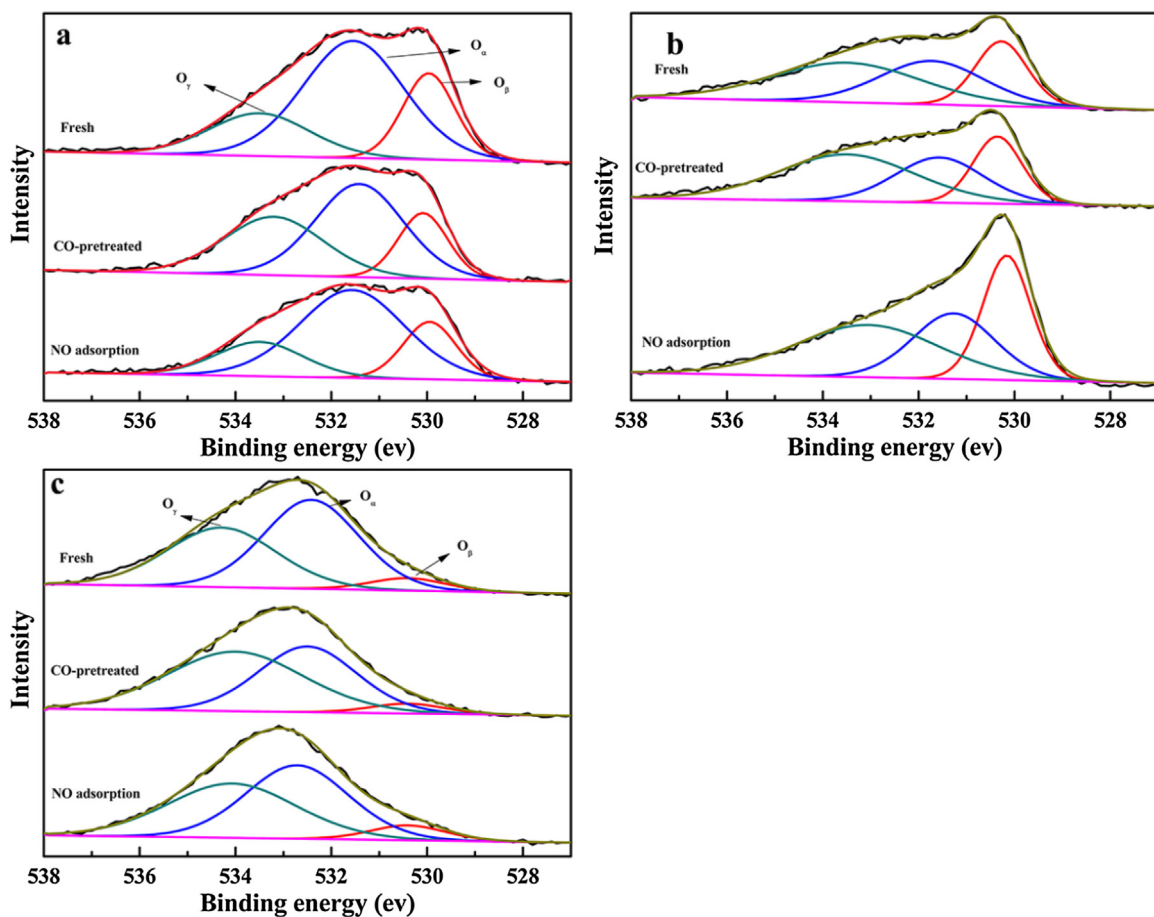


Fig. 6. O 1s from XPS spectra of catalysts (a)  $\text{Fe}_{0.8}\text{Co}_{0.2}/\text{ASC}$ , (b)  $\text{Fe}_{0.8}/\text{ASC}$ , (c)  $\text{Co}_{0.2}/\text{ASC}$  with different treatment.

( $\text{GHSV} = 6000 \text{ h}^{-1}$ ) at  $300^\circ\text{C}$  for 30 min, followed by the introduction of a gas stream with 1000 ppm NO ( $\text{GHSV} = 6000 \text{ h}^{-1}$ ) at  $300^\circ\text{C}$  for 30 min for the adsorption of NO. From the Raman spectra in Fig. 3(b), two bands were observed at  $210 \text{ cm}^{-1}$  and  $470 \text{ cm}^{-1}$ , for fresh  $\text{Fe}_{0.8}\text{Co}_{0.2}/\text{ASC}$ . These bands could be assigned to the characteristic vibrational modes of  $\text{Fe}_2\text{O}_3$  [41–43]. The red-shifts of the  $A_{1g}$  and  $E_g$  modes were observed for these bands, possibly attributed to the addition of Co. The synergistic effect of Fe and Co atoms in the lattice cells possibly induced the distortion of the crystal structure and microscopic stress in the lattice cells [44–46]. A defect was then introduced in the space lattice. Lattice oxygen atoms could easily dissociate from cells to transform to surface adsorption oxygen, resulting in the formation of oxygen vacancies [47,48]. In Fig. 3(b), the characteristic bands disappeared for CO-pretreated  $\text{Fe}_{0.8}\text{Co}_{0.2}/\text{ASC}$ , attributed to the consumption of oxygen atoms in the catalysts by CO, and the oxygen loss resulted in a change of the lattice vibration. After the adsorption of NO on the CO-pretreated catalyst, bands were observed at  $192 \text{ cm}^{-1}$ ,  $442 \text{ cm}^{-1}$ ,  $518 \text{ cm}^{-1}$ , and  $677 \text{ cm}^{-1}$ . Bands observed at  $192 \text{ cm}^{-1}$  and  $442 \text{ cm}^{-1}$  were attributed to the red-shift of  $\text{Fe}_2\text{O}_3$  vibrational modes [41–43], while the band observed at  $518 \text{ cm}^{-1}$  was attributed to the shift of the CoO Raman vibrational modes at  $515 \text{ cm}^{-1}$  [49]. Notably, the band at  $677 \text{ cm}^{-1}$  was assigned to the variation of the CoO lattice vibrational modes at  $684 \text{ cm}^{-1}$  when Fe atoms were introduced into the CoO lattice [50]. For the fresh  $\text{Fe}_{0.8}/\text{ASC}$  catalyst in Fig. 3(c), peaks were observed at  $441 \text{ cm}^{-1}$  and  $489 \text{ cm}^{-1}$ , assigned to  $\text{FeO}$  ( $435 \text{ cm}^{-1}$ ) and Fe ( $498 \text{ cm}^{-1}$ ), in agreement with the XRD analysis [43]. However, CO-pretreatment and NO adsorption resulted in the disappearance of the band at  $489 \text{ cm}^{-1}$ . In Fig. 3(d), characteristic Raman vibrational modes of  $\text{Co}_3\text{O}_4$  (i.e.,  $F_{2g}^1$  mode at  $215 \text{ cm}^{-1}$ ,

$F_{2g}^1$  mode at  $234 \text{ cm}^{-1}$ , and  $E_g$  mode at  $441 \text{ cm}^{-1}$ ) and CoO (i.e.,  $E_g$  mode at  $415 \text{ cm}^{-1}$ ) were detected. Similarly, only bands for the  $F_{2g}^1$  mode of  $\text{Co}_3\text{O}_4$  and vibrational modes of CoO were observed for the catalysts after CO and NO treatment, while other bands disappeared.

In conclusion, when ASC was loaded with only Fe, a low NO conversion was observed; the conversion was slightly below 10%, particularly at low temperatures ( $<250^\circ\text{C}$ ). However, when ASC was loaded with only the Co species, the  $\text{deNO}_x$  efficiency was improved to some extent at low temperatures, but was not sufficient for applications. Moreover, when the optimized binary metals (i.e., Fe and Co) were simultaneously loaded on ASC, the  $\text{deNO}_x$  efficiency was very high, suitable for applications to research. The detection of the microstructure may explain this phenomenon as follows. First, mono-metal loaded on ASC often resulted in metal oxides containing single metal atoms in a lattice cell (e.g.,  $\text{FeO}_x$  or  $\text{Co}_x$ ), which exhibited a weak performance for transferring electrons and catalyzing the rupture of chemical bonds. Single metal atoms in cells led the micro-system to attain a low-energy state; thus, the probability to form defects in the lattice was less [36] than that for binary metal oxides; additionally, there was a lower probability to form oxygen vacancies [20,51]. Nevertheless, an oxygen vacancy generally exhibited a positive charge; hence, it could capture electrons and improve the transfer of electrons. In addition, it could also activate the N–O bond for promoting bond dissociation, thereby catalyzing the reduction of NO. Except that, adsorbed oxygen dissociated from the lattice significantly affected the promotion of CO oxidation. When ASC was doped by Fe and Co oxides, because of mixed crystal effects, Co atoms would be introduced into the lattice of iron oxides; hence, this mixture could significantly

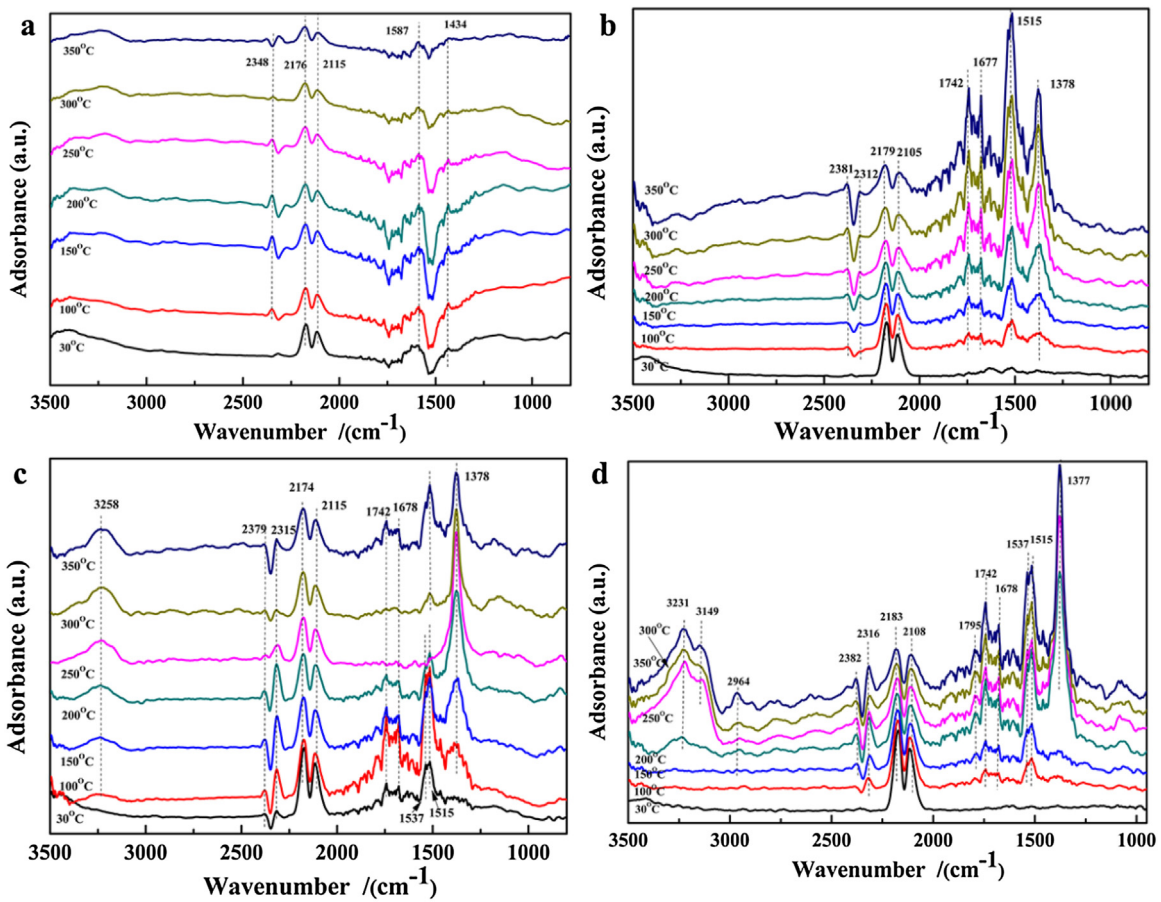


Fig. 7. DRIFTS spectra of (a)  $\text{Fe}_{0.8}\text{Co}_{0.2}/\text{ASC}$ , (b)  $\text{Fe}_{0.8}/\text{ASC}$ , (c)  $\text{Co}_{0.2}/\text{ASC}$ , (d)  $\text{ASC}$  in a flow of 2000 ppm CO at 30, 100, 150, 200, 250, 300, 350 °C.

form defects, which was beneficial for creating oxygen vacancies [47,48]. In this case, SSOVs were produced via the simultaneous loading of Fe and Co on ASC [20], which generally exhibited excellent de $\text{NO}_x$  performance for catalyzing the reaction between NO and CO [20,51].

### 3.5. In situ DRIFTS of $\text{NH}_3$ adsorption

Before the adsorption of  $\text{NH}_3$ , samples were purged by Ar at 400 °C for 1 h, followed by cooling to 100 °C. Then, 1000 ppm of  $\text{NH}_3$  balanced by Ar was introduced into the reaction chamber. Fig. 4 shows the DRIFTS spectra of different catalysts. For the  $\text{Fe}_{0.8}\text{Co}_{0.2}/\text{ASC}$  catalyst, two peaks were observed for 1630  $\text{cm}^{-1}$  and 1450  $\text{cm}^{-1}$ , respectively. For the  $\text{Fe}_{0.8}/\text{ASC}$  catalyst, only one band was observed at 1500  $\text{cm}^{-1}$ . Moreover, for the  $\text{Co}_{0.2}/\text{ASC}$  catalyst and ASC support, no peaks were observed. The adsorption of  $\text{NH}_3$  was less than 200 °C, which was reported to characterize the acid sites of the catalysts. The Brønsted and Lewis acid sites exhibit characteristic bands at 1400–1480  $\text{cm}^{-1}$  [53] and at approximately 1630  $\text{cm}^{-1}$ , respectively [52,54]. According to the spectra,  $\text{Fe}_{0.8}\text{Co}_{0.2}/\text{ASC}$  contained abundant acid sites, including Brønsted acid and Lewis acid sites. However, acid sites were not detected for  $\text{Fe}_{0.8}/\text{ASC}$ ,  $\text{Co}_{0.2}/\text{ASC}$ , and ASC. Li et al. [55] and Nakarin et al. [56] identified that Brønsted acid sites promoted the adsorption of  $\text{NO}_x$ , as well as oxidation and dissociation, which were key steps for the reduction of NO by CO. Hence, the abundant acid sites over the  $\text{Fe}_{0.8}\text{Co}_{0.2}/\text{ASC}$  catalyst contributed to the excellent de $\text{NO}_x$  performance.

### 3.6. XPS analysis

XPS spectra were recorded for some representative samples to further investigate the surface elemental composition and the valence states of iron and cobalt. To explore information regarding the surface ions' valence state variation in the reaction, XPS spectra were also recorded for catalysts treated by CO or NO gas. The XPS analysis of the fresh catalysts was designed to explore the surface original complex, the CO-pretreated catalysts to investigate the reduced surface, and the CO-pretreated (first step) NO-adsorbed (second step) catalysts to obtain the redox performance in the reaction. Fig. 5 shows the spectra of  $\text{Fe}\ 2p_{3/2}$  and  $\text{Co}\ 2p_{3/2}$ . The overlapped peaks were fitted by Gaussian–Lorentzian curves. For the XPS spectra of  $\text{Fe}_{0.8}\text{Co}_{0.2}/\text{ASC}$  (Fig. 5(a)), two major valence states for Fe, i.e.,  $\text{Fe}^{2+}$  and  $\text{Fe}^{3+}$ , were observed, with corresponding binding energies of ~709.4 eV and ~711.3 eV, respectively [42,57,58]. After CO and NO treatment, no obvious change was observed for  $\text{Fe}_{0.8}\text{Co}_{0.2}/\text{ASC}$ . However, for  $\text{Fe}_{0.8}/\text{ASC}$  (Fig. 5(c)), the CO pretreatment possibly resulted in a shift of the main peak of  $\text{Fe}\ 2p_{3/2}$  to a low-valence state, and the NO pretreatment did not revert the low-valence spectrum back to its original position, indicating that NO did not oxidize a low-valence Fe species. During the NO + CO reaction, the Fe species of  $\text{Fe}_{0.8}/\text{ASC}$  changed the valence to a lower state by CO but did not revert back to the high state by NO, i.e., iron oxides tended to be reduced during the reaction. Fig. 5(b) shows the spectrum of  $\text{Co}\ 2p_{3/2}$  in  $\text{Fe}_{0.8}\text{Co}_{0.2}/\text{ASC}$  after different treatments. On the catalyst surface, Co was present in three main valence states:  $\text{Co}^0$ ,  $\text{Co}^{2+}$ , and  $\text{Co}^{3+}$  [59–63]. The complex spectrum of  $\text{Co}\ 2p_{3/2}$  was decomposed into three components:  $\text{Co}^0$  at a binding energy of 778.48 eV,  $\text{Co}^{2+}$  at 780.84 eV, and  $\text{Co}^{3+}$  at 779.4 eV. The

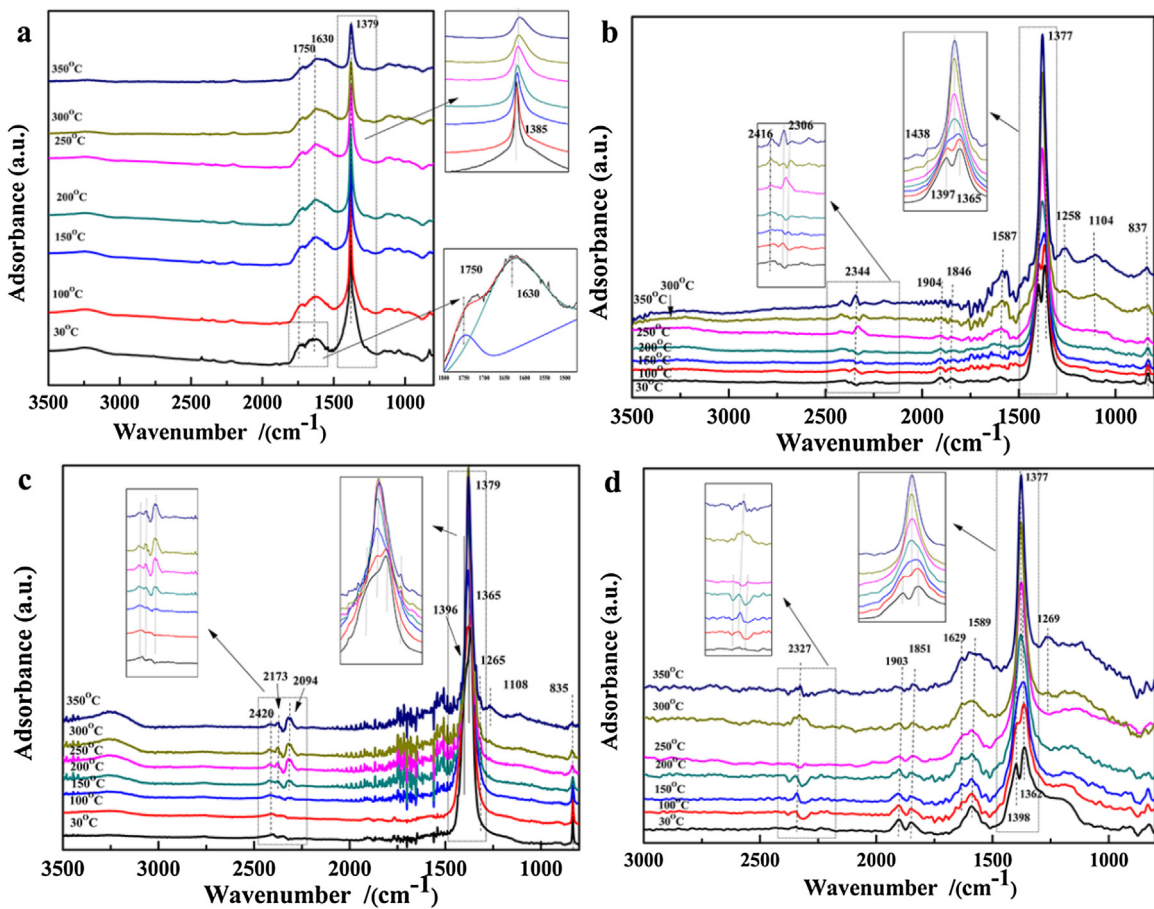


Fig. 8. DRIFTS spectra of (a)Fe0.8Co0.2/ASC, (b) Fe0.8/ASC, (c) Co0.2/ASC, (d) ASC in a flow of 1000 ppm NO at 30, 100, 150, 200, 250, 300, 350 °C.

main peak at 787.6 eV was also assigned to  $\text{Co}^{3+}$ . For  $\text{Co}^{2+}$ , a satellite peak was observed at binding energies of 4.2–6.3 eV greater than the main peak. No satellite peaks were observed for  $\text{Co}^{3+}$ . For the Co 2p3/2 spectra of the  $\text{Fe}_{0.8}\text{Co}_{0.2}/\text{ASC}$  catalyst, two main valence states were observed:  $\text{Co}^{2+}$  and  $\text{Co}^{3+}$ . When the fresh catalyst was pretreated by CO, the binding energy of the main peak shifted to a higher value. The NO treatment shifted the peak back to a position similar to that observed for the fresh catalysts. For  $\text{Co}_{0.2}/\text{ASC}$  (in Fig. 5(d)), no obvious differences were observed for the Co 2p3/2 spectra between fresh and CO-pretreated catalysts. However, after the NO pretreatment, the main peak shifted to a lower binding energy, indicating the transformation of  $\text{Co}^{2+}$  into  $\text{Co}^{3+}$ , which was attributed to NO oxidation. The peaks were fitted as Gaussian–Lorentzian curves, and the fractions of metals in different states were then calculated based on the area of each peak. Table 4 summarizes the calculated values. For  $\text{Fe}_{0.8}\text{Co}_{0.2}/\text{ASC}$ , the valence of Fe species exhibited almost no change after CO and NO treatment; however, the valence of Co significantly changed: the fraction of  $\text{Co}^{3+}$  changed from 55.07% → 32.7% → 45.70% after the CO and NO treatment. The fraction of  $\text{Fe}^{3+}$  in  $\text{Fe}_{0.8}/\text{ASC}$  changed from 45.01% → 32.31% → 31.84%, and the fraction of  $\text{Co}^{3+}$  in  $\text{Co}_{0.2}/\text{ASC}$  changed from 42.07% → 43.47% → 50.42%. Moreover, the corresponding results from the fitting indicated that a portion of  $\text{Co}^{3+}$  was reduced to  $\text{Co}^{2+}$  by CO, and this portion was oxidized to the original state by NO.

From the above XPS study, when only Fe species were loaded on ASC, surface metal oxides were typically reduced in the NO + CO reaction. However, when only the Co species were loaded onto ASC, the surface metal oxides exhibited an opposite trend; the reason for this opposite trend might be because Fe and Co exhibit differ-

ent electronegativities, *i.e.*, the electronegativity values for Fe and Co are 1.83 and 1.88, respectively [64]. When a Co ion was pretreated in a manner similar to the Fe species, the Co ion tended to capture electrons. Thus, during the calcination, the lone-pair electrons of the carbon materials were captured by  $\text{Co}^{2+}$ , resulting in a low-valence state for the Co species.  $\text{Fe}_{0.8}/\text{ASC}$  exhibited a different trend. After CO and NO pretreatment (Fig. 5(a) and (b)),  $\text{Fe}_{0.8}\text{Co}_{0.2}/\text{ASC}$  exhibited stable states for the Fe ion, but the Co ion was subjected to reduction–oxidation. This phenomenon was believed to occur because calcination changed the surface system to a balanced state, *i.e.*, the Fe ion with a relatively higher valence state and the Co ion with a lower state. When CO was adsorbed on the surface, the Fe ion preferentially captured electrons from the adsorbents and then transferred electrons to the Co ion via a special bridge structure: **Fe–O–Co**. With the adsorption of NO, Co ion could transfer electrons to NO, thereby reverting the states back to equilibrium. This inference was consistent with that reported by Lv et al. [20,51], where they proposed that two metal elements containing SSOVs exhibited different change trends for the reaction of NO and CO catalyzed by bi-metal oxides, *i.e.*, one remained stable, while the other changed. Hence, with respect to SSOVs, metals with higher electronegativities exhibited a redox effect, while those with lower electronegativities provided assistance. Furthermore, we speculated that ASC played the support role in the reaction, and the SSOVs were mainly affected by the metals. To prove this, XPS spectra of ASC under different treatments were collected, and the results are listed in Fig. S3. We found that the proportion of the surface chemisorbed oxygen [65,66] did not obviously vary during the reaction (53.95% → 47.89%); this phenomenon was consistent with our speculation.

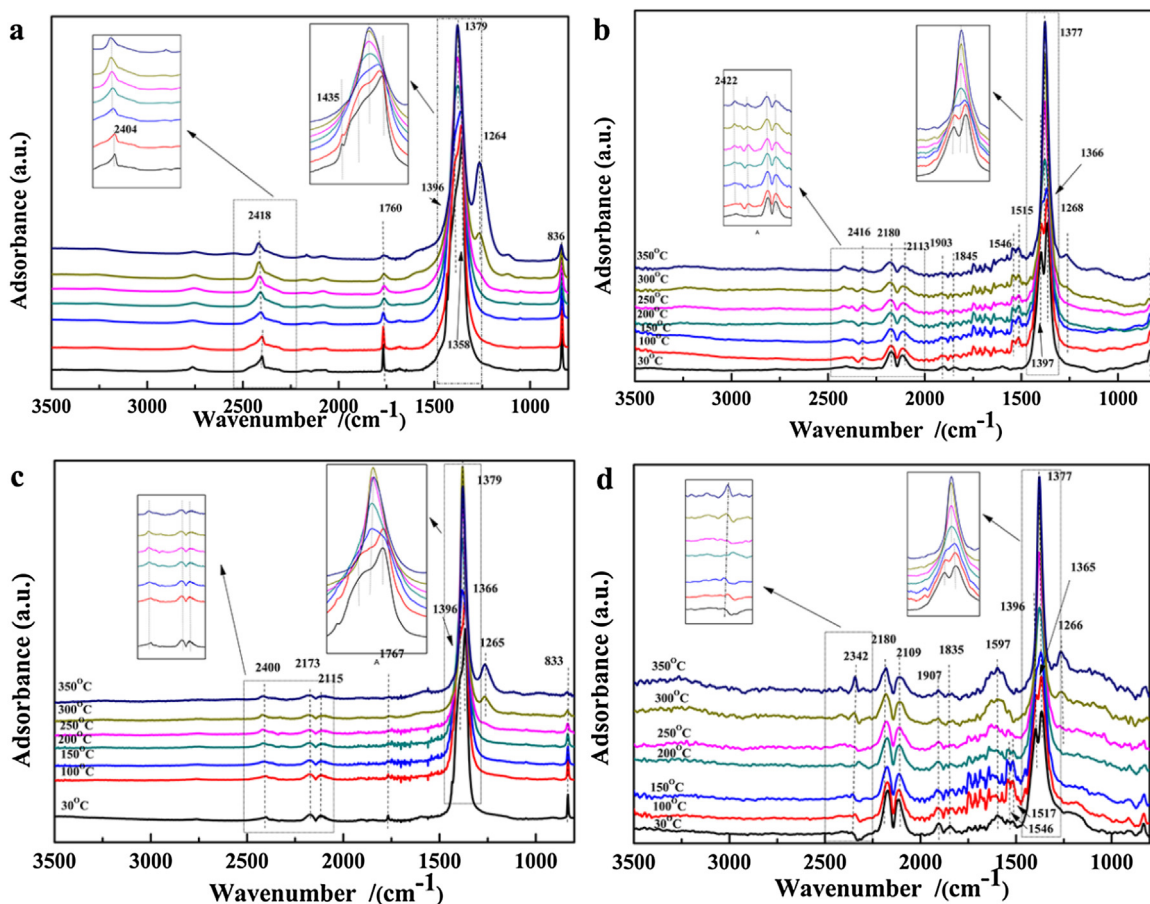


Fig. 9. DRIFTS spectra of (a)  $\text{Fe}_{0.8}\text{Co}_{0.2}/\text{ASC}$ , (b)  $\text{Fe}_{0.8}/\text{ASC}$ , (c)  $\text{Co}_{0.2}/\text{ASC}$ , (d)  $\text{ASC}$  in a flow of 2000 ppm CO + 1000 ppm NO at 30, 100, 150, 200, 250, 300, 350 °C.

**Table 3**  
XPS results of catalysts under different pretreatments.

Catalysts	Pretreatment	Co 2p 3/2			Fe 2p 3/2		O 1s		
		$\text{Co}^0$	$\text{Co}^{2+}$	$\text{Co}^{3+}$	$\text{Fe}^{2+}$	$\text{Fe}^{3+}$	$\text{O}\alpha$	$\text{O}\beta$	$\text{O}\gamma$
$\text{Fe}_{0.8}\text{Co}_{0.2}/\text{ASC}$	Fresh	0.00	44.93	55.07	52.23	42.17	57.37	21.78	20.85
	CO-pretreated	0.00	67.50	32.50	57.83	42.17	47.62	18.75	33.63
	NO adsorption	1.88	52.38	45.70	55.54	44.46	60.54	19.95	19.50
$\text{Fe}_{0.8}/\text{ASC}$	Fresh				54.99	45.01	32.96	24.31	42.74
	CO-pretreated				67.69	32.31	29.18	23.92	46.90
	NO adsorption				68.16	31.84	28.61	31.46	39.94
$\text{Co}_{0.2}/\text{ASC}$	Fresh	1.56	56.37	42.07			53.17	5.88	40.98
	CO-pretreated	0.00	56.53	43.47			42.23	4.75	53.02
	NO adsorption	0.00	49.58	50.42			48.22	7.14	44.64

Fig. 6 shows the XPS spectra of O 1s. Considering the special surface structure of ASC, in this case, the surface oxygen species were categorized into three components: crystal lattice oxygen ( $\text{O}\beta$ ), surface chemical oxygen ( $\text{O}\alpha$ ), and oxygen species in hydroxide groups ( $\text{O}\gamma$ ). According to a previously study,  $\text{O}\beta$  species exhibited binding energies at approximately 529.06–530.4 eV,  $\text{O}\alpha$  exhibited binding energies at 531.1–532.2 eV [65,66], while  $\text{O}\gamma$  exhibited binding energies at 533.5–535.5 eV [67,68]. As shown in Fig. 6, the main peak of O 1s for  $\text{Fe}_{0.8}\text{Co}_{0.2}/\text{ASC}$  was observed in the period of  $\text{O}\alpha$ , while for  $\text{Fe}_{0.8}/\text{ASC}$ , the main peak was skewed in the range of lattice oxygen, possibly attributed to the amount of iron oxide loading. For  $\text{Co}_{0.2}/\text{ASC}$ , the curve center skewed to the period of  $\text{O}\gamma$  species. Table 3 lists the fractions calculated for each species. A high amount of  $\text{O}\alpha$  was observed on the  $\text{Fe}_{0.8}\text{Co}_{0.2}/\text{ASC}$  surface. Yao et al. [9] and Dong et al. [15] suggested that surface chemical oxy-

gen positively affects the catalysis of the NO and CO reaction; the mechanism was likely attributed to the fact that  $\text{O}\alpha$  not only oxidized CO but also promoted the adsorption of NO on the active sites. Furthermore, the amount of  $\text{O}\alpha$  unfortunately decreased after pretreatment with CO. Only  $\text{Fe}_{0.8}\text{Co}_{0.2}/\text{ASC}$  recovered the quantity of  $\text{O}\alpha$ ; this phenomenon indicated that the synergistic effect between Fe and Co promoted the dissociation of NO. The low-temperature catalytic activity of the interaction between NO and CO was highly dependent on the redox performance [9]. According to the XPS spectrum, when bi-metal oxides were loaded on ASC, the redox performance and chemical oxygen increased.

Thus far, it was believed that a special structure, such as  $\text{Fe}-\text{O}-\text{Co}$ , was generated in the metal oxide lattice, and calcination could consume parts of the oxygen from the lattice structure, generating  $\text{Fe}-\square-\text{Co}$ ; this structure could also be generated when

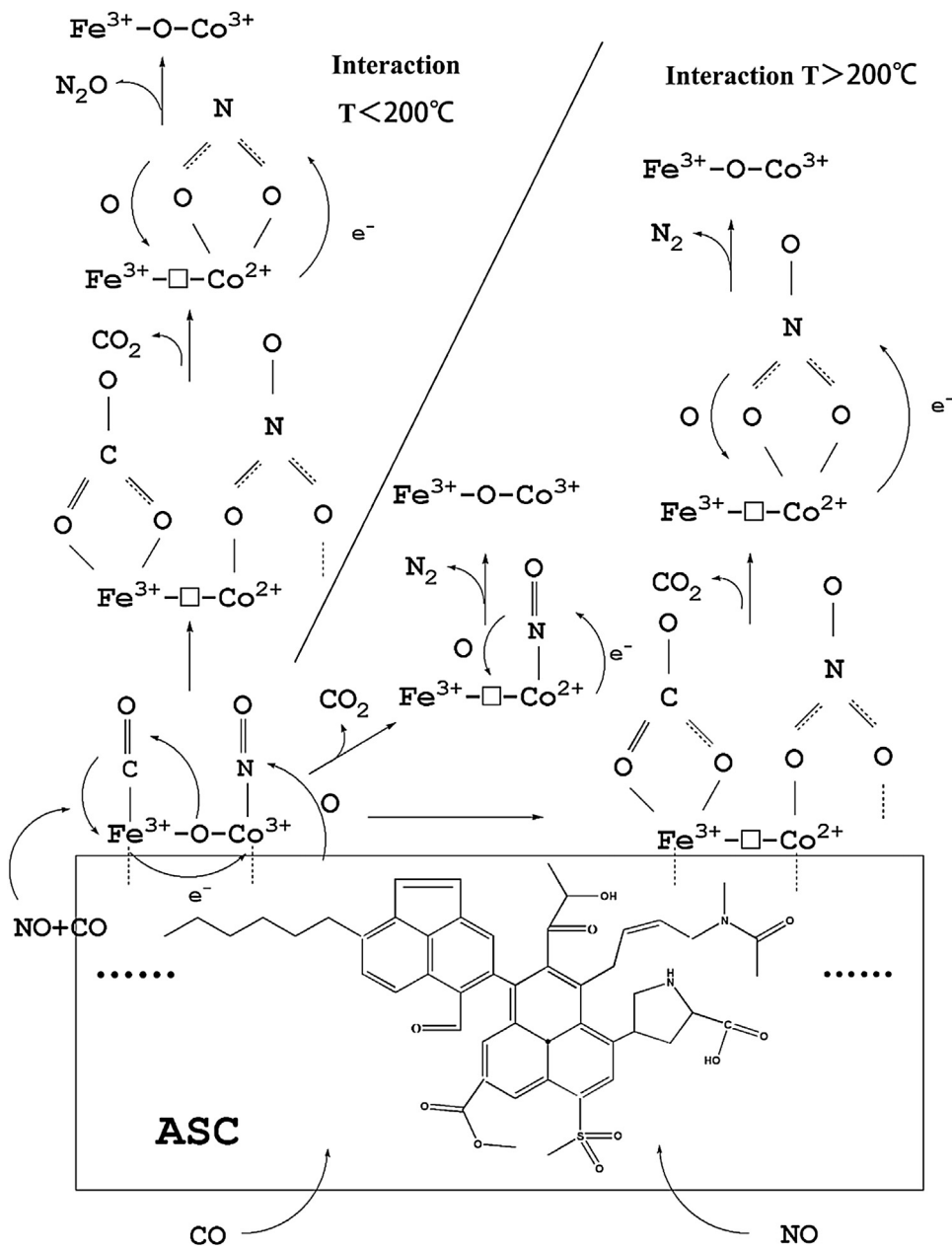


Fig. 10. A possible model for NO reduction by CO over  $\text{Fe}_{0.8}\text{Co}_{0.2}/\text{ASC}$ .

CO reacted with the catalysts by the consumption of some oxygen. Considering the results obtained from the catalytic activity test, this structure resulted in a significant enhancement of the dissociation of NO, affording  $\text{N}_2$ .

### 3.7. Reduction behavior of catalysts ( $\text{H}_2$ -TPR) and ESR results

Fig. S4 shows the  $\text{H}_2$ -TPR profile of the representative catalysts. For ASC, a broad reduction peak was observed at approximately  $622^\circ\text{C}$  with a weak broad peak at approximately  $760^\circ\text{C}$ . The higher-temperature peak was also observed while testing the loaded-type catalysts. The peak at  $760^\circ\text{C}$  was attributed to the interaction between solid carbon and  $\text{H}_2$ , while the low-temperature peak was attributed to the reduction of the carbon oxide complex, such as  $\text{C}-\text{O}$  and  $\text{C}-\text{OH}$  [69,70]. For  $\text{Co}_{0.2}/\text{ASC}$ , a strong peak was observed at  $360^\circ\text{C}$ , with a shoulder peak at approximately  $290^\circ\text{C}$ . Tang et al. [71] proposed that this lower-temperature peak could be assigned

to some non-crystalline  $\text{Co}^{3+}$  species, while the higher-temperature peak could be attributed to the reduction of  $\text{Co}^{3+}$  in  $\text{Co}_2\text{O}_3$  or  $\text{Co}_3\text{O}_4$  [36]. In addition to these two peaks, another obvious reduction peak was observed at  $\sim 583^\circ\text{C}$ , which was assigned to the  $\text{Co}^{2+}$  species. Nevertheless, Tang et al. [36] reported that the characteristic peak for  $\text{Co}^{2+}$  was observed at  $500\text{--}550^\circ\text{C}$ . This phenomenon indicated that an interaction effect existed between Co and ASC at the calcination conditions. For  $\text{Fe}_{0.8}/\text{ASC}$ , in addition to the stronger solid carbon reduction peak, two weaker shoulder peaks were observed at  $480^\circ\text{C}$  and  $578^\circ\text{C}$ , assigned to  $\text{Fe}^{3+}$  and  $\text{Fe}^{2+}$ , respectively. This TPR profile was very distinct from the others, suggesting that some strong Fe-ASC interaction possibly existed during this synthesis.

To further investigate the synergistic effect in  $\text{Fe}_{0.8}\text{Co}_{0.2}/\text{ASC}$ , its TPR profile is displayed in Fig. S4. The peaks were fitted by Gaussian curves using the Origin software. In the original profile, two clear peaks were observed in addition to a shoulder peak. This overlapped peak was decomposed into five peaks. As shown in Fig.

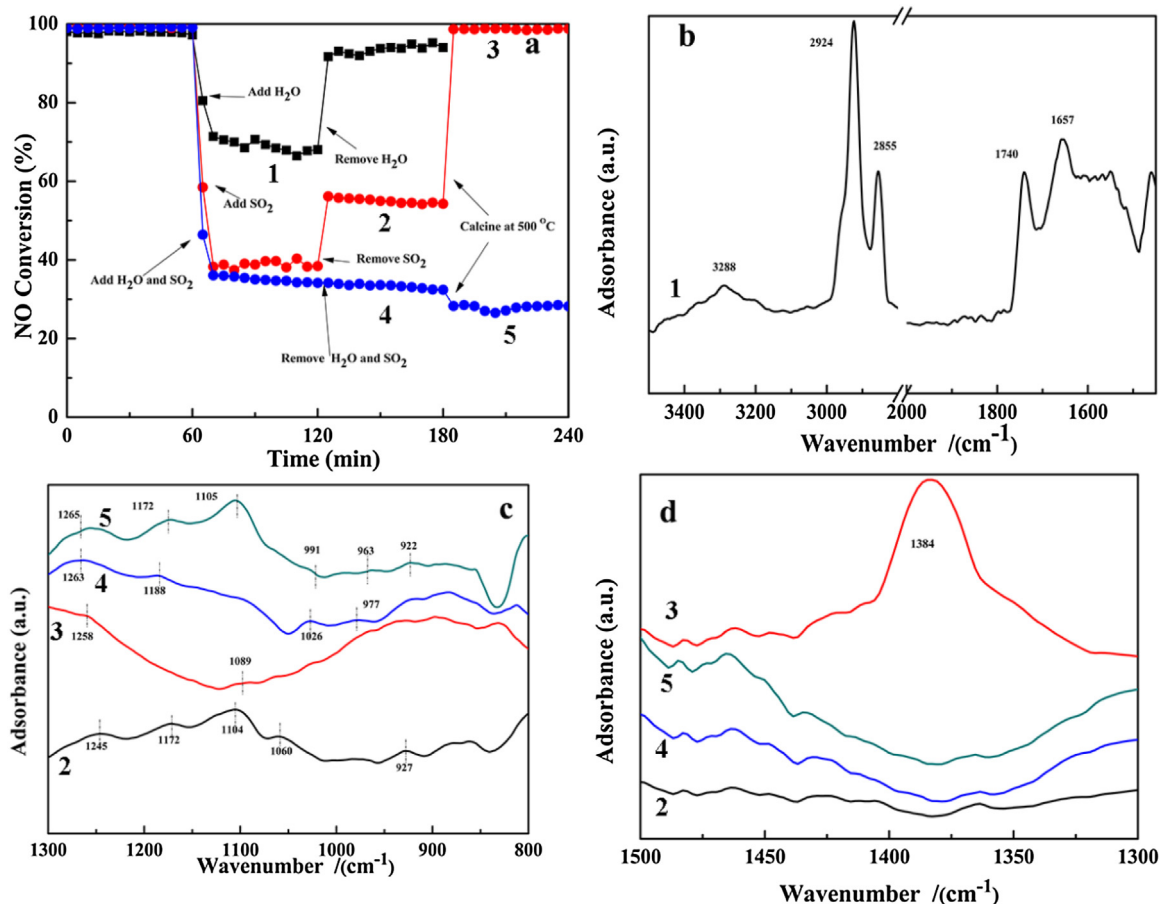


**Fig. 11.** (a) Effects of H<sub>2</sub>O and SO<sub>2</sub> on NO conversion of Fe<sub>0.8</sub>Co<sub>0.2</sub>/ASC, DRIFTS spectra of Fe<sub>0.8</sub>Co<sub>0.2</sub>/ASC with different treatment (b) Reaction in a flow with 10% water gas, (c, d) Reaction in a flow with 1000 ppm SO<sub>2</sub> or 1000 ppm SO<sub>2</sub> + 10% water gas. Reaction conditions: 2000 ppm CO, 1000 ppm NO and balance N<sub>2</sub>, GHSV = 6000 h<sup>-1</sup>.

S4, the central temperature of the characteristic peak, assigned to Co<sup>3+</sup>, shifted from 360 °C to 381 °C; meanwhile, a broad peak was observed at approximately 410 °C, attributed to the shift in the Fe<sup>3+</sup> reduction peak. It was speculated that the shift of these two characteristic peaks was attributed to the interaction between Fe and Co [36,37], i.e., in the surface species, and Section 3.6 shows the proposed Fe–O–Co structures. Besides these peaks, the peak observed at 470 °C was attributed to the reduction of some Co<sup>2+</sup> species in CoO or Co<sub>3</sub>O<sub>4</sub> [36,37,66,72], while the broad peak at 625 °C was assigned to the complex peak of Fe<sup>2+</sup> and carbon oxides species because marginal temperature differences were observed for the reduction peaks of these two components [69,70,73,74].

ESR was performed to investigate the surface oxidation states, the physical form of the transition metal oxides, and some synergistic interactions on the surface. Fig. S5(a) shows the spectra of the representative catalysts. In the spectrum of ASC, only a weak paramagnetic signal was observed at  $g = 1.9987$ . With the loading of Co species, a slightly stronger intensity was observed for this signal; moreover, when Fe and Co were co-loaded on ASC, the intensity of this signal increased. According to previous studies [15,75], the resonance signal at  $g = \sim 2.0033$  was attributed to the existence of lone-pair electrons. For ASC, these electrons existed in the fault or defect of graphite-like crystallite, and for metal-loaded catalysts, the signal was believed to be attributed to the formation of surface oxygen vacancies; these vacancies typically contained a positive charge and could capture unpaired electrons. However, this resonance signal was not observed for Fe<sub>0.8</sub>/ASC, indicating the presence of very few defects. Besides the signal observed at  $g = 1.9987$ , no other signals were observed for ASC,

while a broad resonance signal was detected for all loaded catalysts. For Co<sub>0.2</sub>/ASC, the signal was observed at  $g = 2.4106$ , while for Fe<sub>0.8</sub>/ASC and Fe<sub>0.8</sub>Co<sub>0.2</sub>/ASC, the peaks were observed at  $g = 4.5601$  and  $g = 3.4500$ , respectively. Wichterlová et al. [76] proposed that electrons in the 3d<sup>5</sup> spin orbital exhibited signals at  $g = 3–6$ . Thus, it was speculated that the signal at 4.5601 was attributed to the existence of Fe<sup>3+</sup> [76–78], while the paramagnetic signal at 2.4106 was assigned to Co<sup>3+</sup> species [79]. As for the signal observed at  $g = 3.4500$ , it was speculated that the interaction between Fe and Co caused a shift of this signal. To confirm the interaction of oxygen vacancies and NO, Fe<sub>0.8</sub>Co<sub>0.2</sub>/ASC adsorbed with NO was also detected by ESR. As shown in Fig. S5(b), all signals disappeared for the catalyst treated by NO. For this phenomenon, it was speculated that NO species adsorbed on the surface could coordinate with the active sites, and some electrons could pair with the unpaired electrons in the oxygen vacancies. Thus, from XPS and H<sub>2</sub>-TPR analysis, some special structures, such as SSOVs, were the primary active sites for the NO + CO reaction.

### 3.8. in situ DRIFTS studies on NO or/and CO adsorption

#### 3.8.1. CO adsorption

To further investigate the interaction mechanism between the catalysts surface components and the flue gas composition, *in situ* DRIFTS studies were performed for the adsorption of CO and/or NO on representative catalysts under simulative conditions.

Fig. 7 shows the DRIFTS spectra of CO adsorbed on the catalyst surface with increasing temperature from 30 to 350 °C. For all the tested catalyst samples, two adsorbent peaks were observed

at  $2173\text{ cm}^{-1}$  and  $2120\text{ cm}^{-1}$  at all the tested temperatures; these two bands were assigned to the P and R branches of gaseous CO [8]. With increasing temperature above  $100^\circ\text{C}$ , bands were observed at  $2300\text{--}2400\text{ cm}^{-1}$ , attributed to the formation of physically adsorbed or gaseous  $\text{CO}_2$  [15]. Moreover, as the reaction temperature increasing, the intensity of these bands decreased, attributed to the desorption of physically adsorbed  $\text{CO}_2$ . Fig. 7(a) shows the DRIFTS spectra of  $\text{Fe}_{0.8}\text{Co}_{0.2}/\text{ASC}$ . As can be observed from this figure, except for the peaks mentioned above, two new bands were observed at  $1587\text{ cm}^{-1}$  and  $1434\text{ cm}^{-1}$ , assigned to the vibrational modes of bidentate carbonates ( $1590\text{ cm}^{-1}$ ) [52,80] and monodentate carbonates ( $1435\text{ cm}^{-1}$ ) [8,15] adsorbed on  $\text{Fe}^{3+}$ , respectively. Furthermore, with the temperature increasing, the intensity of the peak at  $1587\text{ cm}^{-1}$  continued to decrease, which was attributed to the decomposition of carbonates. This phenomenon could also demonstrate that some carbonates possibly began to interact with cations, thereby decreasing their valency [8]. Fig. 7(b-d) shows the DRIFTS spectra of other three catalysts, which were distinct. More peaks were observed at  $1350\text{--}1800\text{ cm}^{-1}$ . The bands observed at  $1742\text{ cm}^{-1}$ ,  $1677\text{ cm}^{-1}$ ,  $1515\text{ cm}^{-1}$ , and  $1378\text{ cm}^{-1}$  were assigned to the carbonyl vibration, antisymmetric stretching vibration of bidentate carbonates, as well as the anti-symmetric and symmetric stretching modes of carboxylate radical, respectively. Some other bands were observed at  $1537\text{ cm}^{-1}$  and  $1795\text{ cm}^{-1}$ , attributed to the red-shift of carbonate vibrational modes and carbonyl coupling vibration [8,15,20,81,82]. Moreover, as can be observed from Fig. 7(c and d), at lower temperatures, there was an unobvious peak or no peak at  $1378\text{ cm}^{-1}$  and  $1515\text{ cm}^{-1}$ . With the temperature increasing, the band intensities increased. The results indicated that, on the ASC or  $\text{Fe}_{0.8}/\text{ASC}$  surface, the adsorbed CO reacted with  $\text{O}_2$ , affording carbonate species while simultaneously transferring some electrons to some cation species for reducing their valence states. Ligand bonding between carbonates and reduction species was strong and did not easily decompose, even at higher temperatures. Notably, the band evolution was different for the ASC support and  $\text{Fe}_{0.8}/\text{ASC}$ . Over  $\text{Fe}_{0.8}/\text{ASC}$ , the intensity of the band at  $1515\text{ cm}^{-1}$  was stronger than that at  $1378\text{ cm}^{-1}$  at high temperatures. However, the intensity order was inversed for the ASC support. For  $\text{Co}_{0.2}/\text{ASC}$ , the intensity of the peak at  $1378\text{ cm}^{-1}$  first increased at low temperatures and then decreased at high temperatures, implying that an amount of carboxylates was generated at intermediate temperatures and decomposed at higher temperatures. The bands observed at  $1677\text{ cm}^{-1}$  and  $1742\text{ cm}^{-1}$  significantly increased with temperature over ASC and  $\text{Fe}_{0.8}/\text{ASC}$ , indicating the poor performance to catalyze  $\text{CO}_x$ . However, the same bands over  $\text{Co}_{0.2}/\text{ASC}$  first decreased and then increased. This evolution of bands could be explained by the fact that at lower temperatures, cobalt oxides catalyzed the oxidation of CO, resulting in a decreasing band. With increasing temperature, some carbonates began to decompose, and then with high temperature, some carboxylates were catalyzed, transforming to carbonates and carbonyls.

According to the above analysis, ASC was the main contributor for the adsorption of CO. Iron species could promote  $\text{CO}_x$  formation and weaken their chemical bonds and cobalt species exhibited a major catalytic effect for the decomposition of  $\text{CO}_x$ . On the bi-metal catalyst surface, the synergistic effect promoted the transformation and decomposition of adsorbed carbonate, which could reduce the metal ion valence and enhance NO reduction [20].

### 3.8.2. NO adsorption

To obtain some information about the NO species adsorbed on catalysts, NO adsorption DRIFTS spectra were recorded and are shown in Fig. 8. For  $\text{Fe}_{0.8}\text{Co}_{0.2}/\text{ASC}$  in Fig. 8(a), at a temperature below  $150^\circ\text{C}$ , several peaks were observed at  $1750\text{ cm}^{-1}$ ,

$1630\text{ cm}^{-1}$ , and  $1385\text{ cm}^{-1}$ , assigned to NO weakly adsorbed on  $\text{Co}^{3+}$ , the antisymmetric stretching vibration of bridge bidentate  $\text{NO}_3^-$ , and the antisymmetric stretching vibration of nitro species [8,20,52,83], respectively. With increasing temperature, the band at  $1385\text{ cm}^{-1}$  shifted to  $1379\text{ cm}^{-1}$ , assigned to the characteristic vibration of the free nitrate ion [84]. Furthermore, for the other three catalysts,  $\text{Fe}_{0.8}/\text{ASC}$ ,  $\text{Co}_{0.2}/\text{ASC}$ , and the ASC support in Fig. 8(b-d), respectively, a peak was observed at  $1379\text{ cm}^{-1}$ , indicating that the ASC carrier itself was the important contributor to the adsorption of NO. In Fig. 8(b-d), peaks were observed at approximately  $2400\text{ cm}^{-1}$ , assigned to  $\text{CO}_2$ , implying that adsorbed nitrogen oxides reacted with the surface carbonaceous species on ASC, generating  $\text{CO}_2$ . However, peaks were also observed at  $1365\text{ cm}^{-1}$  and  $1395\text{ cm}^{-1}$ , attributed to the formation of nitrite and nitrate [8,84,85], respectively. With increasing temperature, these two bands shifted to  $1379\text{ cm}^{-1}$  and  $1260\text{--}1270\text{ cm}^{-1}$ , respectively. The latter band was assigned to the vibration mode of chelating bidentate nitrite [8,82]. Peaks were also observed at  $1904\text{ cm}^{-1}$  and  $1846\text{ cm}^{-1}$  over ASC and  $\text{Fe}_{0.8}/\text{ASC}$ , assigned to the characteristic vibration of adsorbed NO linear and bent coordination, respectively [8,20,52,83]. According to Fig. 8(b and c), peaks were observed at  $1120\text{ cm}^{-1}$ ,  $2173\text{ cm}^{-1}$ , and  $2094\text{ cm}^{-1}$ , assigned to the vibration of the nitrosyl species,  $-\text{NCO}$ , and  $\text{N}_2\text{O}$ , respectively, which were intermediates in the  $\text{NO} + \text{CO}$  reaction [20].

In conclusion, we could speculate that, ASC provided sites for the adsorption of some nitrate oxides. The cobalt species played a major role for activating the N–O bond and promoting transformation and decomposition.

### 3.8.3. Co-adsorption of NO and CO

DRIFTS studies for the co-interaction of NO and CO were performed to further investigate the  $\text{CO} + \text{NO}$  reaction mechanism over the representative samples from  $30^\circ\text{C}$  to  $350^\circ\text{C}$ . Fig. 9 shows the results. For all samples, several peaks were observed at  $1200\text{ cm}^{-1}$  to  $1400\text{ cm}^{-1}$ , assigned to the vibration of the free nitrate ion. This result indicated that free nitrates acted as inert species, which were too stable to be reduced by CO during the interaction of  $\text{NO} + \text{CO}$ . Some peaks observed at  $1597\text{ cm}^{-1}$ ,  $1515\text{ cm}^{-1}$ , and  $1546\text{ cm}^{-1}$ , assigned to bidentate carbonates [10,52,83], were also observed in Fig. 9(b and d), but these peaks were not observed in Fig. 9(a and c), indicating that iron species did not promote the decomposition of the species, while cobalt oxides promoted the decomposition of carbonates. In bi-metal catalysts, Fe species predominantly contributed to the adsorption of CO and assisted Co species. By the comparison of these four figures, the cobalt species in the catalysts played a key role in weakening the N–O bond, which could be explained by the shift of the adsorbent wavenumber from  $1907\text{ cm}^{-1}$  or  $1835\text{ cm}^{-1}$  to  $1767\text{ cm}^{-1}$ . Moreover, bands were observed at  $1767\text{ cm}^{-1}$ , assigned to vibrational modes of  $\text{Co}-(\text{NO})_2$ , indicating that Co ions acted as the active site for transforming nitrate oxides, which could promote the key step for the  $\text{NO} + \text{CO}$  reaction, *i.e.*, the dissociation of NO [86]. By the comparison of Figs. 8(a) and 9(a), the peaks observed at  $1630\text{ cm}^{-1}$  disappeared, indicating that bidentate nitrates acted as intermediates during the reaction. According to Figs. 7(a) and 9(a), the peaks corresponding to the CO vibration and bands at  $1587\text{ cm}^{-1}$  were not observed, while the band at  $1434\text{ cm}^{-1}$  disappeared above  $150^\circ\text{C}$ , indicating that the formed carbonates could not be easily generated when NO existed in the flue gas. This result may also imply that carbonates or CO acted as the major intermediate during the  $\text{CO} + \text{NO}$  reaction. It was believed that the high  $\text{N}_2\text{O}$  selectivity at low temperatures was attributed to the decomposition of nitro species.

By summarizing Sections 3.7.1–3, ASC was found to play a major role in the adsorption of NO and CO, while Fe species assisted in the promotion of adsorption and weakening of some chemical

bonds. Moreover, cobalt species played a major role in catalyzing the decomposition of the adsorbents.

### 3.8.4. Mechanism of reaction over $Fe_{0.8}Co_{0.2}/ASC$

The proposed reaction mechanism was based on the XPS, Raman,  $H_2$ -TPR, ESR, and *in situ* DRIFTS experimental observations. A special structure, such as **Fe—O—Co**, was generated during the synthesis of  $Fe_{0.8}Co_{0.2}/ASC$ . However, this structure was unstable in the presence of CO, *i.e.*, CO could consume O, generating an **Fe—□—Co** structure (SSOV), which was crucial for the dissociation of nitrate oxides [8,87]. By analyzing the valence variation of the XPS spectra,  $H_2$ -TPR, and ESR spectra, the majority of SSOVs over  $Fe_{0.8}Co_{0.2}/ASC$  were **Fe<sup>3+</sup>—□—Co<sup>3+</sup>**, which provided the main catalytic activity.

The mechanism for the  $NO + CO$  reaction was as follows: in the mixture flue gas, ASC first adsorbed NO and CO, and then the adsorbed  $CO_x$  species could coordinate with  $Fe^{3+}$ , while NO adsorbents first coordinated with  $Co^{3+}$ . When some surface species, such as  $O_x$ , were involved in the reaction, parts of the coordinated  $CO_x$  could be transformed to bidentate carbonates, while NO adsorbents could be transformed to bidentate nitrate or nitro species. All active coordination was catalyzed by SSOVs, affording  $N_2/N_2O$  and  $CO_2$ . At higher temperature, some CO could directly react with NO when catalyzed by this oxygen vacancy [15]. Fig. 10 shows the possible scheme for the  $NO + CO$  reaction over  $Fe_{0.8}Co_{0.2}/ASC$ .

### 3.9. Effect of $H_2O$ and $SO_2$ on the catalytic performance of $Fe_{0.8}Co_{0.2}/ASC$

The water and  $SO_2$  resistance of  $Fe_{0.8}Co_{0.2}/ASC$  was investigated because this was an important aspect during real applications in the flue gas. The catalysts were also sampled at a specific time during the activity test for further FTIR scanning to explore the reaction mechanism. The results are displayed in Fig. 11.

As shown in Fig. 11 a, in the absence of water, the NO conversion was almost 100% at 250 °C. After 1 h of the  $NO + CO$  reaction, water (10 vol%) was introduced into the flue gas. The inhibition effect of water was obvious, with the conversion decreasing to 80%. However, when water was removed, the efficiency recovered to 95%–98% of the original conversion. According to the FTIR spectra (Fig. 11 b), some bands assigned to the vibration of hydroxyl groups ( $> 2800 \text{ cm}^{-1}$ ) [88,89] and coordinated nitrates ( $1630 \text{ cm}^{-1}$ ) [20] were observed, indicating that water could occupy the active sites that could adsorb NO and CO. Furthermore, the appearance of coordinated nitrate indicated that decomposition was more difficult, *i.e.*, adsorbed water gas could inhibit carbonates from reacting with nitrates.

When 1000 ppm of  $SO_2$  was introduced into the flue gas, the NO conversion drastically decreased. Moreover, the removal of  $SO_2$  could not recover the NO conversion, and only 50% of the original efficiency was attained. As shown in Fig. 11 c, when  $SO_2$  was removed, some bands corresponding to sulfur oxides were still present. Bands were observed at  $1245 \text{ cm}^{-1}$ ,  $1172 \text{ cm}^{-1}$ ,  $1104 \text{ cm}^{-1}$ ,  $1060 \text{ cm}^{-1}$ , and  $927 \text{ cm}^{-1}$  and were assigned to  $\nu_{as}(SO_4^{2-})$ , weakly adsorbed  $SO_2$ ,  $\nu_{as}(S=O)$  of bidentate sulfites,  $\nu_s(SO_4^{2-})$ , and  $\nu(S=O)$  of  $SO_2$ , respectively [89–92]. Another band was observed at  $1384 \text{ cm}^{-1}$ , assigned to  $\nu(NO_3^-)$ . After calcination at 500 °C, the NO conversion mostly recovered. Some bands observed at  $1172 \text{ cm}^{-1}$ ,  $1060 \text{ cm}^{-1}$ , and  $927 \text{ cm}^{-1}$  in the FTIR spectra (Fig. 11 c) disappeared. However, bands assigned to  $\nu(SO_4^{2-})$  at  $1258 \text{ cm}^{-1}$  and  $1080 \text{ cm}^{-1}$  still existed, suggesting that calcination removed some adsorbed  $SO_2$  and sulfites but did not decompose  $SO_4^{2-}$ . Considering NO conversion and FTIR spectra, it was believed that  $SO_2$  was strongly adsorbed by porous carbon materials [93], inhibiting the adsorption of NO.  $SO_2$  adsorbed on the active metal ion transformed into sulfites, resulting in deactivation. Calcination

at 500 °C recovered the catalysts deactivated by sulfites. However, unfortunately, some damage caused by  $SO_4^{2-}$  could not be inhibited; hence, no bands are observed at  $1384 \text{ cm}^{-1}$ .

With the introduction of both  $SO_2$  and water gas, NO conversion was similar to that observed with the introduction of only  $SO_2$ . The catalysts were totally deactivated, and the catalytic activity was not recovered either by the removal of  $SO_2$  and water or by calcination at 500 °C. According to the FTIR spectra, after the introduction of  $SO_2$  and  $H_2O$ , some peaks corresponding to free  $SO_4^{2-}$  ( $1263 \text{ cm}^{-1}$ ), bidentate  $SO_4^{2-}$  ( $1188 \text{ cm}^{-1}$ ), and free  $SO_4^{2-}/HSO_4^-$  ( $977 \text{ cm}^{-1}$ ) [89–91] were observed. Calcination did not remove bands at  $1263 \text{ cm}^{-1}$ . According to a previously reported study [90], this band was assigned to  $\nu(SO_4^{2-})$  in  $Fe_2(SO_4)_3$ . In Figs. 11(c and d), some bands observed at  $1172 \text{ cm}^{-1}$ ,  $1108 \text{ cm}^{-1}$ , and  $900$ – $100 \text{ cm}^{-1}$  were generated by calcination, assigned to coordinated sulfate, indicating that the interaction between water and  $SO_2$  could produce some sulfate species, which resulted in irreversible catalyst deactivation.

To further investigate the surface oxides after exposure to  $H_2O$  and  $SO_2$ , X-ray fluorescence (XRF) testing was performed. The prepared catalysts were also sampled at a specific time (similar to FTIR) to determine the variation of the surface oxides in the adding process, and the corresponding results are listed in Table S1. The  $H_2O$  addition had almost no effects on the surface oxides, while the  $SO_2$  introduction increased the percentage of  $SO_3$  (this instrument can only provide the percentage of  $SO_3$ ). Thus, we could speculate that only  $H_2O$  or only  $SO_2$  might adsorb onto the active site to reduce the NO conversion. Calcination at 500 °C almost recovered the percentage of  $SO_3$  to the original state, demonstrating that  $SO_2$  might only adsorb onto the surface and portion of adsorbed  $SO_2$  had some transforming (readily dissociated sulfites and very little sulfates). The co-addition of  $SO_2$  and  $H_2O$  resulted in the increment of  $SO_3$  compared to “sample 2”, while calcination could only reduce the percentage slightly. This phenomenon may confirm the speculation we proposed based on the FTIR analysis, *i.e.*,  $H_2O$  and  $SO_2$  could interact on the catalyst surface with some sulfates produced.

The reason for water inhibition to the NO conversion was the competitive adsorption between NO and water. Nevertheless, water did not damage the catalyst structure, and deactivation was reversible. The presence of  $SO_2$  generated some sulfites, resulting in reversible catalyst deactivation. The interaction of  $H_2O$  and  $SO_2$  damaged the structure by producing sulfates, resulting in irreversible deactivation.

## 4. Conclusion

After a series of tests on the representative catalysts, the  $NO + CO$  reaction mechanism was revealed over metal-loaded ASC. The conclusions were as follows:

- (1) When ASC as a carrier was loaded by metal oxides for catalyzing the  $NO + CO$  reaction, a mixed crystal effect was observed between the two active metals (Fe and Co) during hydrothermal synthesis. This effect could result in the coexistence of the two metal atoms in the same lattice cell, which would produce microstress in the lattice; the microstress also generated some defects, *i.e.*, lattice oxygen could easily dissociate and transform to chemical adsorbed oxygen, generating a vacancy. Furthermore, these defects made the electronic configuration unstable, resulting in several acid sites. These structural characteristics could contribute to the excellent de $NO_x$  performance of  $Fe_{0.8}Co_{0.2}/ASC$ .
- (2) In the  $NO + CO$  reaction, SSOVs significantly affected catalysis. In SSOVs, metals with a higher electronegativity played the

redox role, while metals with a lower electronegativity served to assist in the reaction.

(3) In the **Fe—□—Co** structure, Co species were the catalytic sites for nitrate oxides, while Fe species were the catalytic sites for CO. However, at low temperatures, Co could catalyze the reaction of NO, resulting in decomposition to N<sub>2</sub>O; hence, Co loading of less than that of Fe was applied. According to the results obtained from *in situ* DRIFTS spectra, at low temperatures (<200 °C), coordinated carbonates reacted with coordinated nitro species, affording CO<sub>2</sub> and N<sub>2</sub>O. However, at higher temperatures (>200 °C), adsorbed NO was transformed to coordinated nitrates, which would react with carbonates, affording N<sub>2</sub> and CO<sub>2</sub>. In addition, adsorbed CO and NO could also directly react.

(4) Water could be competitively adsorbed on the catalyst surface with NO, which would decrease the NO conversion. SO<sub>2</sub> could also be adsorbed by the porous carrier, thereby transforming to sulfites, causing reversible deactivation. The interaction between SO<sub>2</sub> and water produced sulfates, causing irreversible deactivation; this result indicated that the ASC catalysts loaded with Fe and Co used for the NO + CO reaction should be applied in the downstream of desulfurization.

## Acknowledgments

The authors thank the National Natural Science Foundation of China (NO. 51406104), the Fundamental Research Funds of Shandong University (NO. 2014HW024), and the Open Foundation from Key Laboratory of Low-grade Energy Utilization Technologies and Systems in Chongqing University (NO. LLTUTS-201508) for financial support.

## Appendix A. Supplementary data

Supplementary data associated with this article can be found, in the online version, at <http://dx.doi.org/10.1016/j.apcatb.2016.08.021>.

## References

- [1] Z. Liang, X. Ma, H. Lin, Y. Tang, The energy consumption and environmental impacts of SCR technology in China, *Appl. Energ.* 88 (2011) 1120–1129.
- [2] I. Nova, C. Ciardelli, E. Tronconi, D. Chatterjee, B. Bandl-Konrad, NH<sub>3</sub>-SCR of NO over a V-based catalyst: low-T redox kinetics with NH<sub>3</sub> inhibition, *AIChE J.* 52 (2006) 3222–3233.
- [3] X. Cheng, X.T. Bi, Reaction kinetics of selective catalytic reduction of NO<sub>x</sub> by propylene over Fe/ZSM-5, *Chem. Eng. J.* 211 (2012) 453–462.
- [4] T.T. Yang, H.T. Bi, X. Cheng, Effects of O<sub>2</sub>, CO<sub>2</sub> and H<sub>2</sub>O on NO<sub>x</sub> adsorption and selective catalytic reduction over Fe/ZSM-5, *Appl. Catal. B: Environ.* 102 (2011) 163–171.
- [5] X. Cheng, X.T. Bi, Modeling NO<sub>x</sub> adsorption onto Fe/ZSM-5 catalysts in a fixed bed reactor, *Chem. Eng. J.* 211 (2012) 453–462.
- [6] Q. Yu, X. Yao, H. Zhang, F. Gao, L. Dong, Effect of ZrO<sub>2</sub> addition method on the activity of Al<sub>2</sub>O<sub>3</sub>-supported CuO for NO reduction with CO: Impregnation vs. coprecipitation, *Appl. Catal. A: Gen.* 423 (2012) 42–51.
- [7] M. Kacimi, M. Ziyad, L.F. Liotta, Cu on amorphous AlPO<sub>4</sub>: preparation, characterization and catalytic activity in NO reduction by CO in presence of oxygen, *Catal. Today* 241 (2015) 151–158.
- [8] X. Yao, Y. Xiong, W. Zou, L. Zhang, S. Wu, X. Dong, F. Gao, Y. Deng, C. Tang, Z. Chen, L. Dong, Y. Chen, Correlation between the physicochemical properties and catalytic performances of Ce<sub>x</sub>Sn<sub>1-x</sub>O<sub>2</sub> mixed oxides for NO reduction by CO, *Appl. Catal. B: Environ.* 144 (2014) 152–165.
- [9] X. Yao, C. Tang, Z. Ji, Y. Dai, Y. Cao, F. Gao, L. Dong, Y. Chen, Investigation of the physicochemical properties and catalytic activities of Ce<sub>0.67</sub>Mn<sub>0.33</sub>O<sub>2</sub> (M = Zr<sup>4+</sup>, Ti<sup>4+</sup>, Sn<sup>4+</sup>) solid solutions for NO removal by CO, *Catal. Sci. Technol.* 3 (2013) 688–698.
- [10] C. Sun, Y. Tang, F. Gao, J. Sun, K. Ma, C. Tang, L. Dong, Effects of different manganese precursors as promoters on catalytic performance of Cu-O/Mn<sub>2</sub>O<sub>3</sub>/TiO<sub>2</sub> catalysts for NO removal by CO, *Phys. Chem. Chem. Phys.* 24 (2015) 15996–16006.
- [11] T. Chafik, D.I. Kondarides, X.E. Verykios, Catalytic reduction of NO by CO over rhodium catalysts: 1. Adsorption and displacement characteristics investigated by *in situ* FTIR and transient-MS techniques, *J. Catal.* 190 (2000) 446–459.
- [12] W. Shangguan, Y. Teraoka, S. Kagawa, Simultaneous catalytic removal of NO<sub>x</sub> and diesel soot particulates over ternary AB<sub>2</sub>O<sub>4</sub> spinel-type oxides, *Appl. Catal. B: Environ.* 8 (1996) 217–227.
- [13] W. Weisweiler, K. Hizbulah, S. Kureti, Simultaneous catalytic conversion of NO<sub>x</sub> and soot from diesel engines exhaust into nitrogen and carbon dioxide, *Chem. Eng. Technol.* 25 (2002) 140–143.
- [14] B. Reddy, S. Khanna, Self-stimulated NO reduction and CO oxidation by iron oxide clusters, *Phys. Rev. Lett.* 93 (2004) 068301–068301.
- [15] L. Dong, B. Zhang, C. Tang, B. Li, L. Zhou, F. Gong, B. Sun, F. Gao, L. Dong, Y. Chen, Influence of CeO<sub>2</sub> modification on the properties of Fe<sub>2</sub>O<sub>3</sub>–Ti<sub>0.5</sub>Sn<sub>0.5</sub>O<sub>2</sub> catalyst for NO reduction by CO, *Catal. Sci. Technol.* 4 (2014) 482–493.
- [16] L. Simonot, G. Maire, A comparative study of LaCoO<sub>3</sub>, Co<sub>3</sub>O<sub>4</sub> and a mix of LaCo<sub>3</sub>–Co<sub>3</sub>O<sub>4</sub>: II. Catalytic properties for the CO + NO reaction, *Appl. Catal. B: Environ.* 11 (1997) 181–191.
- [17] L. Liu, Y. Chen, L. Dong, J. Zhu, H. Wan, B. Liu, B. Zhao, H. Zhu, K. Sun, L. Dong, Y. Chen, Investigation of the NO removal by CO on CuO–CoO<sub>x</sub> binary metal oxides supported on Ce<sub>0.67</sub>Zr<sub>0.33</sub>O<sub>2</sub>, *Appl. Catal. B: Environ.* 90 (2009) 105–114.
- [18] D. Mehandjiev, M. Khristova, E. Bekyarova, Conversion of NO on Co-impregnated active carbon catalysts, *Carbon* 34 (1996) 757–762.
- [19] D. Mehandjiev, E. Bekyarova, Catalytic neutralization of NO on a carbon-supported cobalt oxide catalyst, *J. Colloid Interf. Sci.* 166 (1994) 476–480.
- [20] Y. Lv, L. Liu, H. Zhang, X. Yao, F. Gao, K. Yao, L. Dong, Y. Chen, Investigation of surface synergistic oxygen vacancy in CuO–CoO binary metal oxides supported on γ-Al<sub>2</sub>O<sub>3</sub> for NO removal by CO, *J. Colloid Interf. Sci.* 390 (2013) 158–169.
- [21] A. Oberlin, Carbonization and graphitization, *Carbon* 22 (1984) 521–541.
- [22] X. Tang, J. Hao, W. Xu, J. Li, Novel MnO<sub>x</sub> catalyst for low-temperature selective catalytic reduction of NO<sub>x</sub> with NH<sub>3</sub>, *Chin. J. Catal.* 27 (2006) 843–848.
- [23] Y. Chen, J. Wang, Z. Yan, L. Liu, Z. Zhang, X. Wang, Promoting effect of Nd on the reduction of NO with NH<sub>3</sub> over CeO<sub>2</sub> supported by activated semi-coke: an *in situ* DRIFTS study, *Catal. Sci. Technol.* 5 (2015) 2251–2259.
- [24] J. Wang, Z. Yan, L. Liu, Y. Zhang, Z. Zhang, X. Wang, Low-temperature SCR of NO with NH<sub>3</sub> over activated semi-coke composite-supported rare earth oxides, *Appl. Surf. Sci.* 309 (2014) 1–10.
- [25] J. Wang, Z. Yan, L. Liu, Y. Chen, Z. Zhang, X. Wang, *In situ* DRIFTS investigation on the SCR of NO with NH<sub>3</sub> over V<sub>2</sub>O<sub>5</sub> catalyst supported by activated semi-coke, *Appl. Surf. Sci.* 313 (2014) 660–669.
- [26] P. Wang, Y. Yu, C. Li, Chen, Study on removal of NO<sub>x</sub> from flue gas by modified semi-coke catalyst at low temperatures, *Ind. Eng. Prog. S1* (2009) 155–158.
- [27] R. Guo, C. Li, Y. Yu, Desulfurization and denitrification of flue gas by semi-coke based sorbent, *Guangzhou Chem. Ind.* 37 (2009) 30–32.
- [28] Q. Xie, X.L. Zhang, Q.R. Chen, G.Z. Gong, Influence of surface modification by nitric acid on the dispersion of copper nitrate in activated carbon, *New Carbon Mater.* 18 (2003) 203–208.
- [29] L. Zhang, C. Li, Y. Hou, L. Wang, Z. Zhai, X. Zhang, Study on absorptive removal of sulfur from FCC gasoline over activated semi-coke adsorbent, *Environ. Chem.* 27 (2008) 301–304.
- [30] J.N. Rosas, J. Rodriguez-Mirasol, T. Cordero, NO reduction on carbon-supported chromium catalysts, *Energ. Fuel.* 24 (2010) 3321–3328.
- [31] J.M. Rosas, R. Ruiz-Rosas, J. Rodriguez-Mirasol, T. Cordero, Kinetic study of NO reduction on carbon-supported chromium catalysts, *Catal. Today* 187 (2012) 201–211.
- [32] S. Stegenga, R. Vansoest, F. Kapteijn, J.A. Moulijn, Nitric-oxide reduction and carbon-monoxide oxidation over carbon-supported copper chromium catalysts, *Appl. Catal. B: Environ.* 2 (1993) 257–275.
- [33] F. Wu, X. Ma, J. Feng, Y. Qian, S. Xiong, 3D-Co<sub>3</sub>O<sub>4</sub> and CoO@C wall arrays: morphology control, formation mechanism, and lithium-storage properties, *J. Mater. Chem. A* 2 (2014) 11597–11605.
- [34] J. Jiang, J. Liu, R. Ding, X. Ji, Y. Hu, X. Li, A. Hu, F. Wu, Z. Zhu, X. Huang, Direct synthesis of CoO porous nanowire arrays on Ti substrate and their application as lithium-ion battery electrodes, *J. Phys. Chem. C* 114 (2009) 929–932.
- [35] S. Nishigaki, S. Yano, H. Kato, T. Hirai, T. Nonomura, BaO–TiO<sub>2</sub>–WO<sub>3</sub> microwave ceramics and crystalline BaWO<sub>4</sub>, *J. Am. Ceram. Soc.* 71 (1988).
- [36] Q. Yang, H. Choi, S.R. Al-Abed, D.D. Dionysiou, Iron-cobalt mixed oxide nanocatalysts: heterogeneous peroxymonosulfate activation, cobalt leaching, and ferromagnetic properties for environmental applications, *Appl. Catal. B: Environ.* 88 (2009) 462–469.
- [37] K. Asami, K. Hashimoto, An XPS study of the surfaces on Fe–Cr, Fe–Co and Fe–Ni alloys after mechanical polishing, *Corros. Sci.* 24 (1984) 83–97.
- [38] D.H. Everett, F.S. Stone, *The Structure and Properties of Porous Materials*, Butterworths, London, 1958, pp. 68–94.
- [39] K.S. Sing, D. Everett, R. Haul, L. Moscou, R. Pierotti, J. Rouquerol, T. Siemieniewska, Reporting physisorption data for gas/solid systems with special reference to the determination of surface area and porosity (Recommendations 1984), *Pure Appl. Chem.* 57 (1985) 603–619.
- [40] Z. Zhang, T. Wang, L. Ke, X. Zhao, C. Ma, Powder-activated semicokes prepared from coal fast pyrolysis: influence of oxygen and steam atmosphere on pore structure, *Energy Fuels* 30 (2016) 896–903.
- [41] D. De Faria, S. Venâncio Silva, M. De Oliveira, Raman microspectroscopy of some iron oxides and oxyhydroxides, *J. Raman Spectrosc.* 28 (1997) 873–878.
- [42] S. Tiwari, R. Prakash, R. Choudhary, D. Phase, Oriented growth of Fe<sub>3</sub>O<sub>4</sub> thin film on crystalline and amorphous substrates by pulsed laser deposition, *J. Phys. D: Appl. Phys.* 40 (2007) 4943–4947.
- [43] J. Shi, G. Wang, X. Wang, Z. Zhang, Raman spectroscopic studies of the rust process on a fresh iron surface, *J. Shanghai Teach. Univ.* 30 (2001) 62–66.

[44] S. Chang, M. Li, Q. Hua, L. Zhang, Y. Ma, B. Ye, W. Huang, Shape-dependent interplay between oxygen vacancies and Ag–CeO<sub>2</sub> interaction in Ag/CeO<sub>2</sub> catalysts and their influence on the catalytic activity, *J. Catal.* 293 (2012) 195–204.

[45] Y. Lou, L. Wang, Z. Zhao, Y. Zhang, Z. Zhang, G. Lu, Y. Guo, Y. Guo, Low-temperature CO oxidation over Co<sub>3</sub>O<sub>4</sub>-based catalysts: significant promoting effect of Bi<sub>2</sub>O<sub>3</sub> on Co<sub>3</sub>O<sub>4</sub> catalyst, *Appl. Catal. B: Environ.* 146 (2014) 43–49.

[46] I. Lopes, N. El Hassan, H. Guerba, G. Wallez, A. Davidson, Size-induced structural modifications affecting Co<sub>3</sub>O<sub>4</sub> nanoparticles patterned in SBA-15 silicas, *Chem. Mater.* 18 (2006) 5826–5828.

[47] S. Carrettin, Y. Hao, V. Aguilar-Guerrero, B.C. Gates, S. Trasobares, J.J. Calvino, A. Corma, Increasing the number of oxygen vacancies on TiO<sub>2</sub> by doping with iron increases the activity of supported gold for CO oxidation, *Chem.-Eur. J.* 13 (2007) 7771–7779.

[48] X. Wei, B. Man, M. Liu, C. Xue, H. Zhuang, C. Yang, Blue luminescent centers and microstructural evaluation by XPS and Raman in ZnO thin films annealed in vacuum, N<sub>2</sub> and O<sub>2</sub>, *Physica B* 388 (2007) 145–152.

[49] H. Liang, L. Zhengcao, Z. Zhengjun, Low-temperature synthesis of single-crystalline Co<sub>3</sub>O<sub>4</sub> nanorods on silicon substrates on a large scale, *Nanotechnology* 19 (2008) 237–243.

[50] H.C. Choi, Y.M. Jung, I. Noda, S.B. Kim, A study of the mechanism of the electrochemical reaction of lithium with CoO by two-dimensional soft X-ray absorption spectroscopy (2D XAS) 2D Raman, and 2D heterospectral XAS-Raman correlation analysis, *J. Phys. Chem. B* 107 (2003) 5806–5811.

[51] L. Zhang, L. Dong, W. Yu, L. Liu, Y. Deng, B. Liu, H. Wan, F. Gao, K. Sun, L. Dong, Effect of cobalt precursors on the dispersion, reduction, and CO oxidation of CoO<sub>x</sub>/Al<sub>2</sub>O<sub>3</sub> catalysts calcined in N<sub>2</sub>, *J. Colloid Interface Sci.* 355 (2011) 464–471.

[52] M.C. Kung, H.H. Kung, IR studies of NH<sub>3</sub>, Pyridine, CO, and NO adsorbed on transition metal oxides, *Catal. Rev. Sci. Eng.* 27 (1985) 425–460.

[53] G. Centi, S. Perathoner, D. Biglino, Adsorption and reactivity of NO on copper-on-alumina catalysts: i. Formation of nitrate species and their influence on reactivity in NO and NH<sub>3</sub> conversion, *J. Catal.* 152 (1995) 75–92.

[54] A. Tsyganenko, D. Pozdnyakov, V. Filimonov, Infrared study of surface species arising from ammonia adsorption on oxide surfaces, *J. Mol. Struct.* 29 (1975) 299–318.

[55] L. Li, N. Guan, HC-SCR reaction pathways on ion exchanged ZSM-5 catalysts, *Micropor. Mesopor.* 117 (2009) 450–457.

[56] N. Mongkolsiri, P. Praserthdam, P. Silveston, R. Hudgins, Transient study of the effect of residual cations in Cu/ZSM-5 for SCR of NO by hydrocarbon, *Chem. Eng. Sci.* 55 (2000) 2249–2256.

[57] T. Yamashita, P. Hayes, Analysis of XPS spectra of Fe<sup>2+</sup> and Fe<sup>3+</sup> ions in oxide materials, *Appl. Surf. Sci.* 254 (2008) 2441–2449.

[58] Z. Qu, L. Miao, H. Wang, Q. Fu, Highly dispersed Fe<sub>2</sub>O<sub>3</sub> on carbon nanotubes for low-temperature selective catalytic reduction of NO with NH<sub>3</sub>, *Chem. Commun.* 51 (2015) 956–958.

[59] A.S. Arico, A.K. Shukla, H. Kim, S. Park, M. Min, V. Antonucci, An XPS study on oxidation states of Pt and its alloys with Co and Cr and its relevance to electroreduction of oxygen, *Appl. Surf. Sci.* 172 (2001) 33–40.

[60] B. Bai, H. Arandiyani, J. Li, Comparison of the performance for oxidation of formaldehyde on nano-Co<sub>3</sub>O<sub>4</sub> 2D-Co<sub>3</sub>O<sub>4</sub>, and 3D-Co<sub>3</sub>O<sub>4</sub> catalysts, *Appl. Catal. B Environ.* S142–143 (2013) 677–683.

[61] Y. Brik, M. Kacimi, M. Ziyad, F. Bozon-Verduraz, Titania-supported cobalt and cobalt-phosphorus catalysts: characterization and performances in ethane oxidative dehydrogenation, *J. Catal.* 202 (2001) 118–128.

[62] P. Bera, H. Seenivasan, K. Rajam, V.W. Grips, Characterization of amorphous Co-P alloy coatings electrodeposited with pulse current using gluconate bath, *Appl. Surf. Sci.* 258 (2012) 9544–9553.

[63] P. Bera, H. Seenivasan, K. Rajam, C. Shrivakumara, S.K. Parida, Characterization and microhardness of Co-W coatings electrodeposited at different pH using gluconate bath: a comparative study, *Surf. Interf. Anal.* 45 (2013) 1026–1036.

[64] K. Li, D. Xue, Estimation of electronegativity values of elements in different valence states, *J. Phys. Chem. A* 110 (2006) 11332–11337.

[65] A.P. Grosvenor, B.A. Kobe, M.C. Biesinger, N.S. McIntyre, Investigation of multiplet splitting of Fe 2p XPS spectra and bonding in iron compounds, *Surf. Interf. Anal.* 36 (2004) 1564–1574.

[66] B. Sexton, A. Hughes, T. Turney, An XPS and TPR study of the reduction of promoted cobalt-kieselguhr Fischer-Tropsch catalysts, *J. Catal.* 97 (1986) 390–406.

[67] J. Sun, C. Ge, X. Yao, Y. Cao, L. Zhang, C. Tang, L. Dong, Preparation of NiO/CeO<sub>2</sub> catalysts by solid state impregnation and their application in CO oxidation, *Acta Phys.-Chim. Sin.* 29 (2013) 2451–2458.

[68] M. Alifanti, B. Baps, N. Blangenois, J. Naud, P. Grange, B. Delmon, Characterization of CeO<sub>2</sub>–ZrO<sub>2</sub> mixed oxides. Comparison of the citrate and sol-gel preparation methods, *Chem. Mater.* 15 (2003) 395–403.

[69] M. Roman-Martinez, D. Cazorla-Amorós, A. Linares-Solano, C.S.-M. De Lecea, TPD and TPR characterization of carbonaceous supports and Pt/C catalysts, *Carbon* 31 (1993) 895–902.

[70] A. Calafat, J. Laine, A. López-Agudo, J. Palacios, Effect of surface oxidation of the support on the thiophene hydrodesulfurization activity of Mo, Ni, and NiMo catalysts supported on activated carbon, *J. Catal.* 162 (1996) 20–30.

[71] C. Tang, C. Wang, S. Chien, Characterization of cobalt oxides studied by FT-IR, Raman, TPR and TG-MS, *Thermochim. Acta* 473 (2008) 68–73.

[72] H. Vantblik, D. Koningsberger, R. Prins, Characterization of supported cobalt and cobalt-rhodium catalysts. III. temperature-programmed reduction (TPR), oxidation (TPO), and EXAFS of cobalt-rhodium/silica, *J. Catal.* 97 (1986) 210–218.

[73] G. Munteanu, L. Ilieva, D. Andreeva, Kinetic parameters obtained from TPR data for  $\alpha$ -Fe<sub>2</sub>O<sub>3</sub> and systems, *Thermochim. Acta* 291 (1997) 171–177.

[74] L.I. Ilieva, D.H. Andreeva, A.A. Andreev, TPR and TPD investigation of Au/ $\alpha$ -Fe<sub>2</sub>O<sub>3</sub>, *Thermochim. Acta* 292 (1997) 169–174.

[75] L. Jing, Y. Zheng, Z. Xu, F. Dong, X. Sun, W. Cai, Y. Xu, Electronic paramagnetic resonance characteristic of ZnO ultrafine particles and their photocatalytic performance, *Chem. J. Chin. Univ.* 22 (2001) 1885–1888.

[76] B. Wichterlová, P. Jiru, ESR study of Fe<sup>3+</sup>-zeolites, *React. Kinet. Catal. L.* 13 (1980) 197–201.

[77] A.V. Kucherov, M. Shelef, Quantitative determination of isolated Fe<sup>3+</sup> cations in Fe-HZSM-5 catalysts by ESR, *J. Catal.* 195 (2000) 106–112.

[78] E. Possenriede, O.F. Schirmer, H.J. Donnerberg, G. Godefroy, A. Maillard, ESR identification of Fe containing defects in BaTiO<sub>3</sub>, *Ferroelectrics* 92 (1989) 245–252.

[79] L. Yang, C. Yin, Y. Jiao, L. Zhang, Spectrum structure and g factor of electron paramagnetic resonance of LiCoO<sub>2</sub> crystal doped with Ni, *Acta Phys. Sin.* 55 (2006) 1991–1996.

[80] P.G. Harrison, E.W. Thornton, Tin oxide surfaces. part 9-Infrared study of the adsorption of CO, NO and CO+NO mixtures on tin (IV) oxide gels containing ion-exchanged Cr III, Mn II, Fe III, Co II, Ni II and Cu II, *J. Chem. Soc. Faraday Trans. 1* (74) (1978) 2703–2713.

[81] Y. Denkwtz, B. Schumacher, G. Kučerová, R.J. Behm, Activity, stability, and deactivation behavior of supported Au/TiO<sub>2</sub> catalysts in the CO oxidation and preferential CO oxidation reaction at elevated temperatures, *J. Catal.* 267 (2009) 78–88.

[82] K.I. Hadjiivanov, Identification of neutral and charged N<sub>x</sub>O<sub>y</sub> surface species by IR spectroscopy, *Catal. Rev.* 42 (2000) 71–144.

[83] Y. Xiong, X. Yao, C. Tang, L. Zhang, Y. Cao, Y. Deng, F. Gao, L. Dong, Effect of CO-pretreatment on the CuO-V<sub>2</sub>O<sub>5</sub>/Al<sub>2</sub>O<sub>3</sub> catalyst for NO reduction by CO, *Catal. Sci. Technol.* 4 (2014) 4416–4425.

[84] G. Zhou, B. Zhong, W. Wang, X. Guan, B. Huang, D. Ye, H. Wu, *In situ* DRIFTS study of NO reduction by NH<sub>3</sub> over Fe-Ce-Mn/ZSM-5 catalysts, *Catal. Today* 175 (2011) 157–163.

[85] X. Gu, H. Li, L. Liu, C. Tang, F. Gao, L. Dong, Promotional effect of CO pretreatment on CuO/CeO<sub>2</sub> catalyst for catalytic reduction of NO by CO, *J. Rare Earth.* 32 (2014) 139–145.

[86] A.G. Makeev, N.V. Peskov, The reduction of NO by CO under oxygen-rich conditions in a fixed-bed catalytic reactor: a mathematical model that can explain the peculiar behavior, *Appl. Catal. B: Environ.* 132 (2013) 151–161.

[87] C. Ge, L. Liu, Z. Liu, X. Yao, Y. Cao, C. Tang, F. Gao, L. Dong, Improving the dispersion of CeO<sub>2</sub> on gamma-Al<sub>2</sub>O<sub>3</sub> to enhance the catalytic performances of CuO/CeO<sub>2</sub>/gamma-Al<sub>2</sub>O<sub>3</sub> catalysts for NO removal by CO, *Catal. Commun.* 51 (2014) 95–99.

[88] L. Cheng, X.P. Ye, A DRIFTS study of catalyzed dehydration of alcohols by alumina-supported heteropoly acid, *Catal. Lett.* 130 (2009) 100–107.

[89] G. Xie, Z. Liu, Z. Zhu, Q. Liu, J. Ge, Z. Huang, Simultaneous removal of SO<sub>2</sub> and NO<sub>x</sub> from flue gas using a CuO/Al<sub>2</sub>O<sub>3</sub> catalyst sorbent: II. Promotion of SCR activity by SO<sub>2</sub> at high temperatures, *J. Catal.* 224 (2004) 42–49.

[90] B.Q. Jiang, Z.B. Wu, Y. Liu, S.C. Lee, W.K. Ho, DRIFT study of the SO<sub>2</sub> effect on low-temperature SCR reaction over Fe- Mn/TiO<sub>2</sub>, *J. Phys. Chem. C* 114 (2010) 4961–4965.

[91] G. Xie, Z. Liu, Z. Zhu, Q. Liu, J. Ge, Z. Huang, Simultaneous removal of SO<sub>2</sub> and NO<sub>x</sub> from flue gas using a CuO/Al<sub>2</sub>O<sub>3</sub> catalyst sorbent: i. Deactivation of SCR activity by SO<sub>2</sub> at low temperatures, *J. Catal.* 224 (2004) 36–41.

[92] Q. Wu, H. Gao, H. He, Study SO<sub>2</sub> effect on the selective catalytic reduction of NO<sub>x</sub> with propane over Ag/Al<sub>2</sub>O<sub>3</sub> by *in situ* DRIFTS, *Chin. J. Catal.* 27 (2006) 403–408.

[93] Z. Zhang, T. Wang, C. Ma, T. Feng, T. Ma, Effect of oxygen concentration on activated char pore structure during low oxygen fast pyrolysis, *J. China Coal Soc.* 39 (2014) 2107–2113.